Chemical Engineering Science 253 (2022) 117545

Contents lists available at ScienceDirect

Chemical Engineering Science

journal homepage: www.elsevier.com/locate/ces

Effect of grid-screen on bubble characteristics of vertically discharged bubble plumes

Arsalan Behzadipour [a], Amir H. Azimi [b,*], Iran E. Lima Neto [c]

[a] Dept. of Civil Engineering, Lakehead University, Thunder Bay, ON P7B 6A9, Canada
[b] Dept. of Civil Engineering, Lakehead University, Thunder Bay, ON P7B 5E1, Canada
[c] Dept. of Hydraulic and Environmental Engineering, Federal University of Ceara, Brazil, Pici Campus, Bl. 713, 60455-900, Brazil

HIGHLIGHTS

- The effect of grid-screen on the mixing capacity of bubble plumes was tested.
- The grid-screen can reduce the vertical velocity of bubbles by 38%.
- Bubble concentration increased by 9% as the distance after grid-screen increased.
- The effect of grid-screen became negligible at a certain distance after the screen.
- Bubble size growth after the grid-screen is correlated with Reynolds number.

ARTICLE INFO

Article history:
Received 23 September 2021
Received in revised form 1 February 2022
Accepted 18 February 2022
Available online 24 February 2022

Keywords:
Bubble plume
Air–water mixing
Bubble dynamics
Bubble size
Bubble velocity
Bubble breakup
Coalescence

ABSTRACT

A series of laboratory experiments was conducted to improve the entrainment and mixing capacity of vertically discharged bubble plumes by employing a grid-screed with different openings and at different distances from the nozzle. Bubble characteristics such as bubble size, bubble size distribution, bubble concentration, and bubble velocity were measured using an accurate Refractive Bubble Index (RBI) probe along the plume, before, and after the grid-screen. The effects of grid-screen openings and airflow discharge on variations of bubble characteristics were examined. Experimental results showed that the size of grid-screen and its distance from the nozzle decreased the vertical velocity of bubbles by an average of 38%. Dynamics of bubbles before and after the grid-screen was analyzed and a regime classification was proposed based on variations of the normalized bubble velocity with the distance from the nozzle. It was found that increasing the distance between the grid-screen and nozzle increased bubble concentration by approximately 9% and reduced bubble size by 31%. At a certain distance from the nozzle, the effect of the grid-screen became negligible and bubble velocity reached its initial value. This specific distance was extracted for all tests and the results showed that such critical distance was correlated with the nozzle Reynolds number. Empirical correlations were developed to estimate the effective mixing length after the grid-screen. The proposed equations were found to be correlated with the bubble Reynolds number.

1. Introduction

Multi-phase bubble plumes have been utilized in industrial technologies, natural water reclamation, and water quality improvement due to their capacity to induce buoyancy-driven flows and promote aeration and mixing. They have been recognized as an efficient method of enhancing air/oxygen transfer in lakes, rivers, and wastewater treatment plants (Wüest et al., 1992a; Simiano et al., 2006; Funaki et al., 2009; Paerl and Otten, 2013; Aoyama et al., 2016; Ibelings et al., 2016; Yang et al., 2016). The advantages of bubble plumes over mechanical mixing systems are the simplicity of design, affordability of construction, and operation costs (Pacheco and Lima Neto, 2017; Lima and Lima Neto, 2018). Bubble plumes have been utilized in many environmental engineering problems such as oxygenation of the hypolimnion layer in lakes to reduce phosphorus release from sediments, and inhibit algal growth (Soltero et al., 1994, Moura et al., 2020). Other common applications of bubble plumes are in oxygenation of sewage in wastewater treatment plants (Schladow, 1992, 1993), in de-stratification of lakes and reservoirs

* Corresponding author.
E-mail addresses: abehzadi@lakeheadu.ca (A. Behzadipour), azimi@lakeheadu.ca (A.H. Azimi), iran@deha.ufc (I.E. Lima Neto).

https://doi.org/10.1016/j.ces.2022.117545
0009-2509/

(Lima Neto et al., 2016), in mixing of very hot or toxic liquids (Aoyama et al., 2016), and in destratification of lakes and reservoirs (Bormans et al., 2016). Moreover, air injection into effluent diffusers can be also an attractive alternative for artificial aeration of water bodies (Lima Neto et al., 2007).

Several mechanisms control the motion of bubbles in stagnant ambient such as initial momentum due to airflow, nozzle size, initial buoyancy due to density difference between air and water, and turbulent diffusion due to bubble motion (Lima Neto, 2012). Air is released from porous diffusers, single circular nozzles or a cluster of nozzles to form a bubbly jet/plume, resulting in bubbles with different shapes, sizes, and velocities depending on the discharge device and the initial airflow discharge. Hence, the initial flow configurations such as nozzle size and airflow rate are indispensable to understand, control, and simulate such jets/plumes (Yapa et al., 1999; Socolofsky and Adams, 2002, 2003; McGinnis et al., 2004; Singleton et al., 2007; Lima Neto et al., 2008a; Mantripragada et al., 2021). A forced plume or a buoyant jet is formed when air and water are injected through a nozzle in which both momentum and buoyancy forces control the motion of bubbles (Lee and Chu, 2003; Lima Neto et al., 2008b). In bubbly jet-plumes, bubbles move upward due to the density difference between air and water, and bubble motion is augmented by the initial injection of air and water. Extensive experimental and numerical studies have been performed to understand bubble dynamics and different models were proposed to predict bubble dynamics and mixing in bubbly jets and plumes.

Experimental studies have shown that the geometry and initial flow rates of air/water have significant importance in the characteristics of bubble plumes (Rosso and Stenstrom, 2006; Lima Neto et al., 2008a; Laupsien et al. 2017; Lai and Socolofsky, 2019; Liu et al., 2019). Table 1 shows a list of experimental studies to explore the dynamics of bubble plumes for mixing improvement by testing the controlling parameters such as nozzle size, d_o, airflow rate, Q_o, mean bubble diameter, d_b, and ambient water depth, h.

Many research studies have demonstrated the effect of air injection on the hydrodynamics of bubbles in multiphase plumes and have correlated the initial parameters such as nozzle size and air discharge on variations of bubble centerline velocity (Milgram, 1983; Socolofsky and Adams, 2003, 2005; Bombardelli et al., 2007; Lima Neto et al., 2008a, 2012; Wang et al., 2019; Besbes et al., 2020; Bohne et al., 2020). Fisher and Honda (1979) indicated that the centerline velocity of bubbles in momentum-driven bubble plumes is a function of distance from the nozzle, x, and the initial momentum flux, M_o. In buoyancy-driven plumes (i.e., buoyant plumes) the centerline velocity of the plume is a function of distance from the nozzle, x, and the initial buoyancy flux, B_o. Recent studies have also confirmed the nonlinear correlation between the centerline velocity of bubbles and the distance from the nozzle in form of $u_b \sim x^{-1/3}$ (Bombardelli et al. 2007; Lai and Socolofsky, 2019). Bombardelli et al. (2007) provided a prediction model to estimate bubble centerline velocity, u_s, by scaling the distance from the nozzle, x, with a length scale, D, at which $D = gQ_o/4\pi\alpha^2 u_s^3$ where g is the acceleration due to gravity, α is the entrainment coefficient, and u_s is the bubble slip velocity. It was found that the normalized bubble velocity can be expressed as $u_b/u_s = 1.24\,(x/D)^{-1/3}$.

The impact of bubble expansion as hydrostatic pressure decreases and buoyancy variation were studied by Fannelop (1980). The centerline velocity of bubbles and its variations along with a relatively deep tank (i.e., $h = 10$ m) was measured and the effect of air discharge, ranged between 300 L/min to 1326 L/min, on bubble velocity was tested. It was found that the centerline bubble velocity decreased with distance from the nozzle, x, and the centerline velocity linearly decreased by 34% at a distance 9 m from the nozzle. A series of experimental investigations was carried out to study the effects of plume configuration on model blowout and broken gas pipelines (Milgram, 1983). Their laboratory experiments were carried out in a 3.66 m deep tank and bubble plumes with different air discharges ranging between 12.1 L/min and 140 L/min were tested. It was found that the centerline velocity of bubbles decreased by approximately 45% at a distance 1.5 m from the nozzle and velocity variations along the vertical axis became negligible afterwards.

Experimental studies on the aeration configuration of bubble plumes have shown that the initial nozzle configuration has a negligible effect on variations of centerline bubble velocity (Lima Neto et al., 2008a). Lima Neto (2012) developed an integral model to predict bubble velocity variations and found that the centerline velocity was invariant with water depth for $x > 1.5$ m. Beyond the threshold distance, the centerline velocity of bubbles was 34% of the initial bubble velocity. Fraga et al. (2016) performed a large-eddy simulation of bubble plumes. The numerical model was validated with the experimental data of vertically released bubble plumes (see Table 1). An adverse correlation was found between bubble size and centerline velocity. It was found that the slope of velocity decay decreased with increasing mean bubble diameter. The numerical results indicated that the centerline bubble velocity decreased far from the nozzle and it was independent of the nozzle size.

Wang et al. (2019) developed a new theoretical study based on diffusive spreading to describe the lateral spreading of bubble plumes. The proposed theoretical study was validated with experimental data. Bubble plume characteristics such as bubble mean velocity, volume flux, momentum flux, and spreading rate of bubble plumes were predicted for buoyancy-driven (i.e., pure plume) and weak momentum-driven bubble plumes. The spreading rate of the weak momentum-driven plumes was found to be smaller than the classic buoyancy-driven pure plume. The dynamics of weak momentum-driven bubble plumes indicated that the normalized bubble velocity decreased with a distance from the nozzle in form of $u_b/u_s \sim x^{-1/2}$.

Many studies have shown the effect of plume characteristics such as nozzle diameter and airflow rate on bubble size and bubble size distributions (Clift et al., 1978; Iguchi et al., 1989; Wüest et al., 1992b; Swasn and Mores, 1993; Rensen and Roig, 2001; Bergmann et al., 2004; García and García, 2006; Lima and Lima Neto, 2008; Bryant et al., 2009; Ziegenhein and Lucas, 2017a,b; Lima and Lima Neto, 2018; Niida and Watanabe, 2018). Laboratory experiments indicated that bubble breakup occurs at a threshold Reynolds number of $Re = 8000$. For $Re > 8000$, large bubbles break up into smaller bubbles and produce a relatively uniform bubble size distribution (Lima Neto et al., 2008b; Laupsien et al., 2021). It was found that bubble velocity was independent of nozzle size, but bubble size decreased by approximately 20% to 50% for bubble plumes generated from porous air-stone instead of single circular nozzles.

Recent laboratory experiments have confirmed the effect of porous diffusers on altering the variations of centerline bubble velocity with depth (Li et al., 2020). The numerical simulations of Li et al. (2020) have revealed that bubble size distribution ranged between 1 mm and 1.5 mm at the center of the plume and bubble sizes increased from 1.5 mm to 2.5 mm along the axis of the plume. Relatively larger bubbles (i.e., 2.5 mm < d_b < 3 - mm) were observed on the boundary of the plume. The experimental study of Ziegenhein and Lucas (2017)a,b showed an adverse correlation between bubble size and airflow rate. It was reported that bubble plumes with high flow rates generated a more uniform bubble size distribution. The recent study of Bohne et al. (2020) confirmed the adverse correlation between bubble size and airflow rate.

Table 1
Experimental parameters and air flow discharges of bubbly jets and plumes from the literature.

No.	Study	Flow	Tank Size (m) $W \times L \times H$	h (m)	d_o (mm)	Q_o (L/min)	d_b (mm)
1	Asaeda and Imberger (1993)	Bubble plume	1 × 1 × 0.75	0.38–0.6	24	0.00264–0.768	< 4
2	Rensen and Roig (2001)	Bubble plume	0.15 × 0.15 × 0.67	0.465	Capillary tube	1.26	2.8
				0.465		1.84	3
				0.465		3.24	3.4
				0.65		1.84	3
3	Bergmann et al. (2004)	Bubble plume	0.4 × 0.4 × 0.7	0.7	Air stone	0.5, 1, 1.5	3
4	Roig and De Tournemine (2007)	Bubbly jet	0.3 × 0.15 × 3.1	3.1	Capillary tube	Q_a = 0.4–5	1.14–2.38
						Q_w = 1–7	
5	Seol et al. (2007)	Bubble plume	0.38 × 0.38 × 0.8	0.6	Air stone	0.5	1.51
						1	1.71
						1.5	2.02
6	Lima Neto et al. (2008a)	Bubble plume	1.2 × 1.2 × 0.8	0.76	1 × 6	2, 3	8
					1 × 3		
					4 × 1.5		
					9 × 1		
					Air stone		
7	Lima Neto et al. (2008b)	Bubbly jet, Pure water jet	1.2 × 1.2 × 0.8	0.76	4, 6, 9, 13.5	Q_a = 7.56–108	1.14–2.38
						Q_w = 12	
8	Lima Neto et al. (2008d)	Bubbly jet	1.8 × 1.2 × 0.8	0.76	6	Q_a = 1, 3, 5	1.8–3.4
						Q_w = 3, 5, 7	
9	Seol et al. (2009)	Bubble plume	0.38 × 0.38 × 0.8	0.7	Air stone	0.1	1.2
10	Riboux et al. (2010)	Bubble plume	0.15 × 0.15 × 1	1	0.1	Not reported	1.6
					0.2		2.1
					0.33		2.5
					0.4		2.5
11	Bryant et al. (2009)	Bubble plume	1 × 2 × 1.5	1.5	Air stone	0.5, 1, 1.5	2
12	Funaki et al. (2009)	Bubble plume	1 × 1 × 1	1	127	Not reported	0.3–5.8
13	Fraga and Stoesser (2016)	Bubble plume	2 × 1 × 1	1	Air stone	0.5, 1.5	1, 2, 4
14	Ziegenhein and Lucas, 2017	Bubble plume	0.05 × 0.25 × 0.6	0.6	0.7–0.9	0.6	3–5
			0.05 × 0.1125 × 1.8	1.8		4.81	7–8
15	Alméras et al. (2017)	Bubble plume	0.45 × 0.45 × 2	2	Capillary tube	Not reported	2–3.6
16	Lima and Lima neto (2018)	Bubbly jet	0.5 × 0.5 × 1	0.8	1 × 30	Q_a = 1–9	1.7–4.8
					1 × 10	Q_w = 11–30	
					4 × 5		
					8 × 3.5		
17	Niida and Watanabe (2018)	Bubble plume	0.15 × 0.17 × 0.2	0.2	0.26	0.015	2
					0.4	0.04	3.2
					1.2	0.05	3.6
					1.2	0.08	4.2
					1.2	0.012	4.9
18	Lai and Socolofsky (2019)	Bubble plume	1 × 1 × 1	1	Air stone	0.5, 1.5	1–4
19	Wang et al. (2019)	Bubble plume	9.1 × 4.6 × 16.8	16.8	0.4	0.25	3.8
						1.2	4.1
20	Besbes et al. (2020)	Bubble plume	0.25 × 0.25 × 0.3	0.3	Sparger	850	4.55
						2550	4.87
						4250	4.88
21	This study	Bubble plume	0.85 × 1.60 × 0.80	0.7	1, 3	4, 6, 8	6–14

A novel Micro Structured Bubble Column reactor (MSBC) was designed by using a wire mesh structure inserted in a pseudo-2D bubble column reactor (Sujatha et al., 2015). Different bubbly flow configurations passing through the wire mesh were tested by employing visual observations. The experimental results identified three different regimes named as bubble cutting, bubble cutting followed by re-coalescence, and gas pocket formation. The superficial gas velocities for different mesh sizes ranged from 5 to 50 mm/s. In addition to image analysis, an ultrafast X-ray tomography technique was employed to study the effect of wire mesh on bubble size reduction (Sujatha, 2016).

The performance of Micro Structured Bubble Column on bubble dynamics was investigated numerically (Jain et al., 2013). The results of validated numerical model to simulate MSBC indicated that the wire meshing is able to cut the bubbles, increases the interfacial area of bubbles, and enhances the interface dynamics. The effects of single layer and double layers of mesh on bubble dynamics were tested by employing optical measurements and

Particle Image Velocimetry (PIV) techniques (Chen et al., 2021). A comparison between one and two layers of mesh with the benchmark tests indicated that the bubble size decreased by 22.7% and 29.7%, the gas hold up increased by 5.7% and 9.7%, and the interfacial area increased by 34.8% and 43.5%, respectively.

The present study is motivated by the effect of porous air-stone devices in reducing bubble size and increasing the contact area between air and water in buoyancy-driven bubble plumes. The larger contact surface between air and water enhances the oxygen transfer between air and water, which is beneficial in improving effluent quality in wastewater treatment plants and can improve the efficiency of aerators in natural water bodies (Mueller et al., 2002a,b). Due to presence of small porous media in air-stone nozzles, such devices are more susceptible to clogging in wastewater treatment tanks and require frequent backwash and maintenance. To reduce the operation cost because of significant head losses in porous nozzles and the maintenance costs due to clogging of air-stones over time, a grid-screen is introduced which is installed at fixed distances from a single circular nozzle.

In this study, two grid-screens with different opening dimensions are tested and the grid-screens are installed at three different distances from the nozzle. The variations of bubble size, bubble concentration, and velocity along the vertical axis of the bubble plumes are measured for different air discharges to understand how air discharge and screen size affect bubble characteristics and how far air bubbles remain intact after passing through a grid-screen. To test the effects of controlling parameters such as nozzle size, airflow rates, grid-screen openings, and the distance between grid-screen and nozzle on the efficiency of bubble plume after the grid-screen, the variations of bubble characteristics such as size, velocity, and concentration with the design parameters are examined.

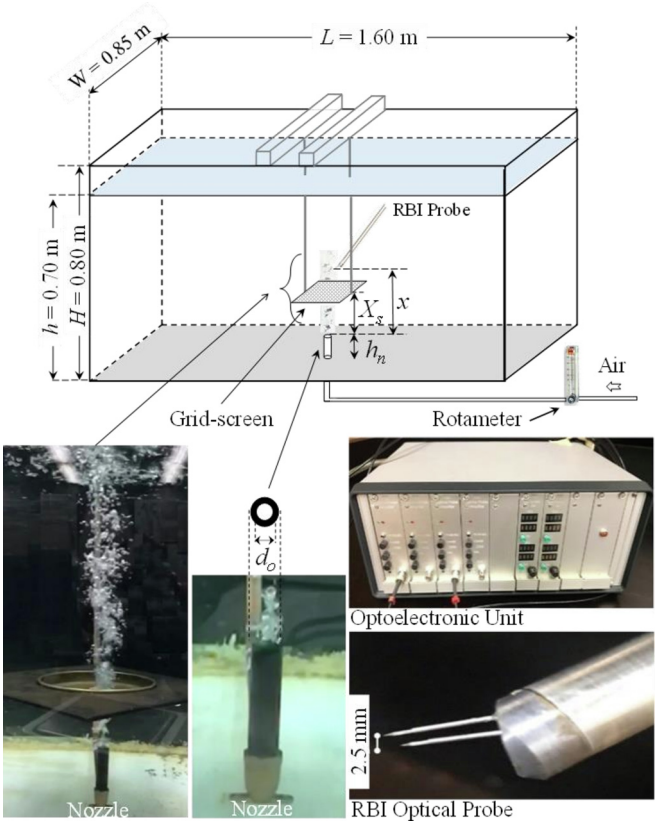

Fig. 1. The schematic of experimental setup, image of bubbly plume passing through a grid-screen, the components of an optoelectronic unit and Refractive Bubble Instrument (RBI) optical probe tip.

1.1. Experimental setup

A series of laboratory experiments were conducted in the Multiphase Flow Research Laboratory (MFRL) at Lakehead University to study the effects of air discharge and grid-screen on variations of bubble characteristics. The experiments were performed in a glass-walled tank of 1.60 m long, 0.85 m wide, and 0.80 m deep as shown in Fig. 1. The tank was filled up with tap water at 20 °C ± 1 °C to a depth of 0.70 m. An air pipeline provided compressed air with a pressure of $P = 4$ atm. Different airflow rates of $Q_a = 4$ L/min, 6 L/ min, and 8 L /min were selected for this study. The airflow rates were measured with an accurate rotameter (LZM series Zyia OEM, Zhejiang, China) with an accuracy of ± 4%. Two different circular nozzles with the inner diameters of $d_o = 1$ - mm and 3 mm were chosen and the nozzles were placed at the center of the tank and at 100 mm above the bottom (see Fig. 1). Standard grid-screens with sieve openings of $d_s = 0.841$ mm (i.e., sieve number #20) and $d_s = 2.380$ mm (i.e., sieve number #16) were employed. The grid-screen was installed at three different elevations from the nozzle, $X_s = 0.14$ m, 0.22 m, and 0.30 m.

Overall, 36 experiments were carried out to test the effects of nozzle size, d_o, air discharge, Q_a, grid-screen size, d_s, and the distance between grid-screen and the nozzle, X_s (see Table 2). Benchmark tests (i.e., bubble plumes without a grid-screen) were performed to evaluate the performance of grid-screens on bubble size and velocity reduction. The optical probe was placed at the centerline of the nozzle and measurements were taken in a vertical axis from the nozzle to the water surface with an increment of 30 mm. The experimental parameters, bubble characteristics, and the associated non-dimensional parameters are listed in Table 2. The time averaged bubble velocity and concentration were calculated from the analog voltage signals by the RBI software. In Table 2, u_b is the bubble velocity, d_a is the bubble size, C_b is the concentration factor, and Re is the Reynolds number at the nozzle in which $Re = u_o d_o / \upsilon_{air}$, where u_o is the initial bubble velocity, d_o is the nozzle diameter, and υ_{air} is the kinematic viscosity of air.

The experimental tests started with BP, which stands for Bubble Plume, and the numbers after BP are the nozzle size in millimeter, air discharge in L/min, and sieve number. For example, the test BP1-4–20 belongs to a bubble plume with a nozzle diameter of $d_o = 1$ mm, air discharge of $Q_a = 4$ L/min, and the sieve number of #20. In this study, bubble characteristics such as bubble size, bubble velocity, and void fraction are measured.

A high-resolution camera (Prosilica GT 1910c CCD, Germany) with a speed of 20 frames per second was placed perpendicular to the tank with 1.4 m from the tank to capture images of bubble plumes and break-up/coalescence of bubbles before and after the grid-screen. A snapshot of bubble plume after the grid-screen is shown in Fig. 1. The camera was fitted with either a 90-mm Kowa F 1.8 (Kowa, Japan) or an 18–55 mm AF-Sinkkor, 13.5–5.6 GII (Nikon, Japan) lens. A double-tip optical fiber probe system (RBI instrumentation, Meylan, France) was used to measure bubble characteristics such as bubble size, bubble velocity, and bubble concentration. A module emits infrared light via two fiber-optic cables to the tips of the probe. The probes' tips are 15 mm long, 2.5 mm apart, and two sapphire crystals were installed at the end of the probe tips (see Fig. 1). The emitted light is refracted when the probe tip is in water and is reflected in the module when the probe tip is in the air (i.e., inside a bubble). The reflected light passes through a semi-transparent mirror combined with a prism towards a photosensitive diode in the module. The light transmission system enables the probe to acquire voltage signals with a sampling rate of 1 MHz (RBI User Manual, Meylan, France).

Table 2
Experimental parameters and bubble characteristics of vertically discharged bubble plumes passing through a sieve.

Test NO.	Test.	X	d_o	Q_a	Sieve No/size		X/do	u_b (m/s)	d_b	C_b	Re
	symbol	(mm)	(mm)	(L/min)	No.	(mm)		(m/s)	(mm)	(%)	(-)
1	BP1-4	0	1	4	–	–	–	0.855	8.94	3.98	5661.71
2	BP1-6	0	1	6	–	–	–	0.96	10.57	4.74	8492.56
3	BP1-8	0	1	8	–	–	–	1.085	10.4	9.05	11323.42
4	BP3-4	0	3	4	–	–	–	0.76	9.22	3.67	1887.23
5	BP3-6	0	3	6	–	–	–	0.846	10.32	4.59	2830.85
6	BP3-8	0	3	8	–	–	–	1.12	13.64	5.85	33,970
7	BP1-4–16	14	1	4	16	2.38	3.50	0.734	7.63	4.02	5661.71
8	BP1-4–16	22	1	4	16	2.38	5.50	0.68	7.56	3.27	5661.71
9	BP1-4–16	30	1	4	16	2.38	7.50	0.66	7.43	2.89	5661.71
10	BP1-6–16	14	1	6	16	2.38	2.33	0.797	7.68	5.46	8492.56
11	BP1-6–16	22	1	6	16	2.38	3.67	0.73	7.24	4.37	8492.56
12	BP1-6–16	30	1	6	16	2.38	5.00	0.698	7.26	4.19	8492.56
13	BP3-4–16	14	3	4	16	2.38	3.50	0.688	6.82	3.94	1887.23
14	BP3-4–16	22	3	4	16	2.38	5.50	0.65	6.9	3.38	1887.23
15	BP3-4–16	30	3	4	16	2.38	7.50	0.62	6.8	3.36	1887.23
16	BP3-6–16	14	3	6	16	2.38	2.33	0.769	7.36	5.24	2830.85
17	BP3-6–16	22	3	6	16	2.38	3.67	0.727	7.12	4.63	2830.85
18	BP3-6–16	30	3	6	16	2.38	5.00	0.67	6.86	4.1	2830.85
19	BP1-4–20	14	1	4	20	0.841	3.50	0.676	7.42	2.64	5661.71
20	BP1-4–20	22	1	4	20	0.841	5.50	0.61	7.22	1.965	5661.71
21	BP1-4–20	30	1	4	20	0.841	7.50	0.54	6.45	1.64	5661.71
22	BP1-6–20	14	1	6	20	0.841	2.33	0.78	7.57	4.49	8492.56
23	BP1-6–20	22	1	6	20	0.841	3.67	0.73	7.56	3.99	8492.56
24	BP1-6–20	30	1	6	20	0.841	5.00	0.65	7.03	3.24	8492.56
25	BP1-8–20	14	1	8	20	0.841	1.75	0.89	7.63	7.01	11323.42
26	BP1-8–20	22	1	8	20	0.841	2.75	0.86	7.86	7.24	11323.42
27	BP1-8–20	30	1	8	20	0.841	3.75	0.78	7.34	6.34	11323.42
28	BP3-4–20	14	3	4	20	0.841	3.50	0.73	7.22	3.7	1887.23
29	BP3-4–20	22	3	4	20	0.841	5.50	0.58	6.65	1.86	1887.23
30	BP3-4–20	30	3	4	20	0.841	7.50	0.5	5.96	1.54	1887.23
31	BP3-6–20	14	3	6	20	0.841	2.33	0.81	7.67	5.03	2830.85
32	BP3-6–20	22	3	6	20	0.841	3.67	0.67	6.99	3.42	2830.85
33	BP3-6–20	30	3	6	20	0.841	5.00	0.62	6.84	3.22	2830.85
34	BP3-8–20	14	3	8	20	0.841	1.75	0.89	8.16	6.48	33,970
35	BP3-8–20	22	3	8	20	0.841	2.75	0.77	7.65	5.38	33,970
36	BP3-8–20	30	3	8	20	0.841	3.75	0.67	7.96	5.34	33,970

The raw signals are directly amplified and detected through a threshold technique method (ISO Lite Software, RBI Optical probe, France) and the analog signals are converted to a two-state signal corresponding to the phases of air and water as shown in Fig. 2. Fig. 2 shows a sample of a two-stage voltage signal during 30 s of data acquisition and a sketch of the phase identification. By analyzing digital voltage signals, the double-tip optical fiber probe is capable of measuring bubble size, void fraction (i.e., bubble concentration), and bubble frequency. In addition, bubble velocities are calculated by cross-correlation of voltage signals from both probe tips. The RBI double-tip optical fiber probe has been successfully employed in many studies. The accuracy and robustness of the system have been verified in measuring bubble characteristics in two-phase gas–liquid flows (Rensen and Roig, 2001; Boes and Hager, 2003; Kiambi et al., 2003; Chaumat et al., 2005; Murzyn et al., 2005; Lima Neto et al., 2008a,b,c). However, the RBI double-tip optical fiber probe has limitation in size determination of very oblong bubbles. A careful observation of the images in the present study indicated that the bubbles were mostly semi-spherical.

A number of research papers evaluated the performance of Double Optical Probe over other measurement techniques such as Passive Acoustics, Inverted Funnel, and Image Analysis (Vazquez et al., 2005; Kiambi et al., 2003). Vazquez et al. (2005) investigated the performance of three measurement techniques for bubble size determination in the quiescent water. The Passive Acoustic method performed within an accuracy between 97% and 99% in comparison with the Inverted Funnel method having an accuracy range

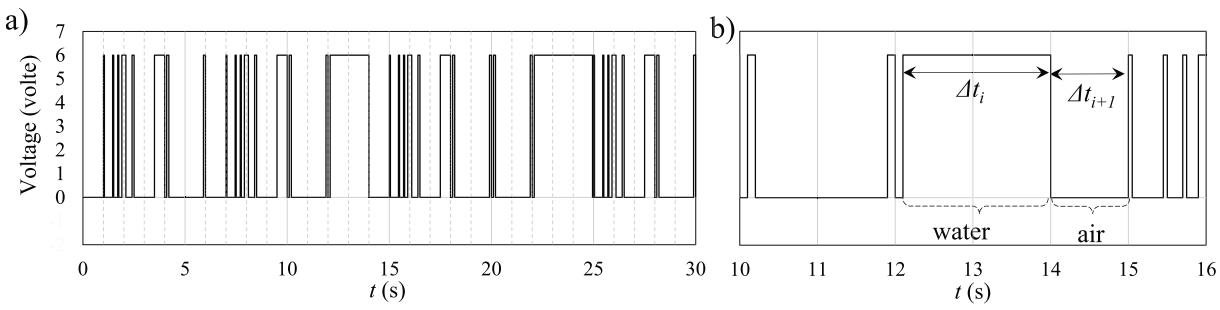

Fig. 2. Time histories of the recorded voltage signals with a Refractive Bubble Instrument (RBI) optoelectronic unit: a) a sample of instantaneous voltage signals with time; b) phase identification from raw voltage signals.

between 88% and 96%. Furthermore, a comparison between Double Optical Probe and Image Analysis indicated that the RBI Optical Probe results were more accurate in bubble characteristics measurements especially in highly unidirectional flows where the bubble translations and rotations effects are minimized by the ambient flow (Kiambi et al., 2003).

2. Results and discussions

Fig. 3 shows the time histories of the cumulative averages for bubble velocity and bubble concentration for Tests No. 1 and No. 7 (i.e., bubble plumes with and without a grid-screen). A recording time duration of 120 s was selected for all experiments to ensure reaching suitable average values of bubble characteristics. The black dashed lines show the time averaged bubble velocity and concentration at 120 s from the beginning of measurements. The red dashed lines show the ± 5% variations from the averaged bubble velocity and concentration for 120 s of data. For bubble plumes without a grid-screen, the averaged bubble velocity and concentration after 120 s duration of data were 0.791 m/s and 3.917%, respectively. The cumulative average values of bubble velocity and concentration for bubble plumes with a grid-screen indicated that the bubble velocity and bubble concentration decreased by 12.5 % and 7.5%, respectively.

To ensure the repeatability of results, the test with Q_a = 8 L/min, d_o = 3 mm, and the test with Q_a = 8 L/min, d_o = 1 mm were repeated three times. The bubble size and normalized bubble velocity had the measurement uncertainty of + 1.5% and −2.5 %, respectively. Moreover, the same method was applied to find the uncertainty for boundary height and normalized bubble diameter between regimes (III) and (IV) with the measurement uncertainty of + 3.4% and −4.3 %, respectively.

2.1. Flow visualization

Fig. 4 shows the snapshot images of bubble plumes without a grid-screen for different airflow discharges. The time interval between each consecutive image is two seconds. As the airflow discharge increased from 4 L/min to 8 L/min, a cloud of bubbles was developed and large air pockets were formed due to the wake effect behind the frontier air cloud, which reduces the rate of oxygen transfer along the vertical axis of the plume.

Fig. 5 shows a comparison between the images from bubble plumes with and without a grid-screen for Q_a = 4 L/min and d_o = 1 - mm. The grid-screen has an opening size of 0.841 mm and it was located 0.14 m above the nozzle. Fig. 5a shows a snapshot image of a bubble plume without a grid-screen and Fig. 5b shows the snapshot image of the same bubble plume with a grid-screen. Five close-up images were selected along the vertical axis of the bubble plume to compare the effect of grid-screen on the shape and size of the air pockets. As can be seen in the close-up images, the air pockets in bubble plume with a grid-screen break up into a cluster of smaller bubbles which the clusters of small bubbles increase the air–water contact surfaces and, as a result, enhances the oxygen transfer.

2.2. Time history data

Fig. 6 shows the effect of grid-screen on the time-history of bubble concentration at the plume centerline and at x/d_o = 330, where x is the distance from the nozzle to the point of measurement. The dashed line in Fig. 6 shows the time averaged concentration for a period of three minutes. The nozzle diameter and air discharges were 1 mm and 4 L/min, respectively. A comparison between the bubble plume without a grid-screen (Fig. 6a) and

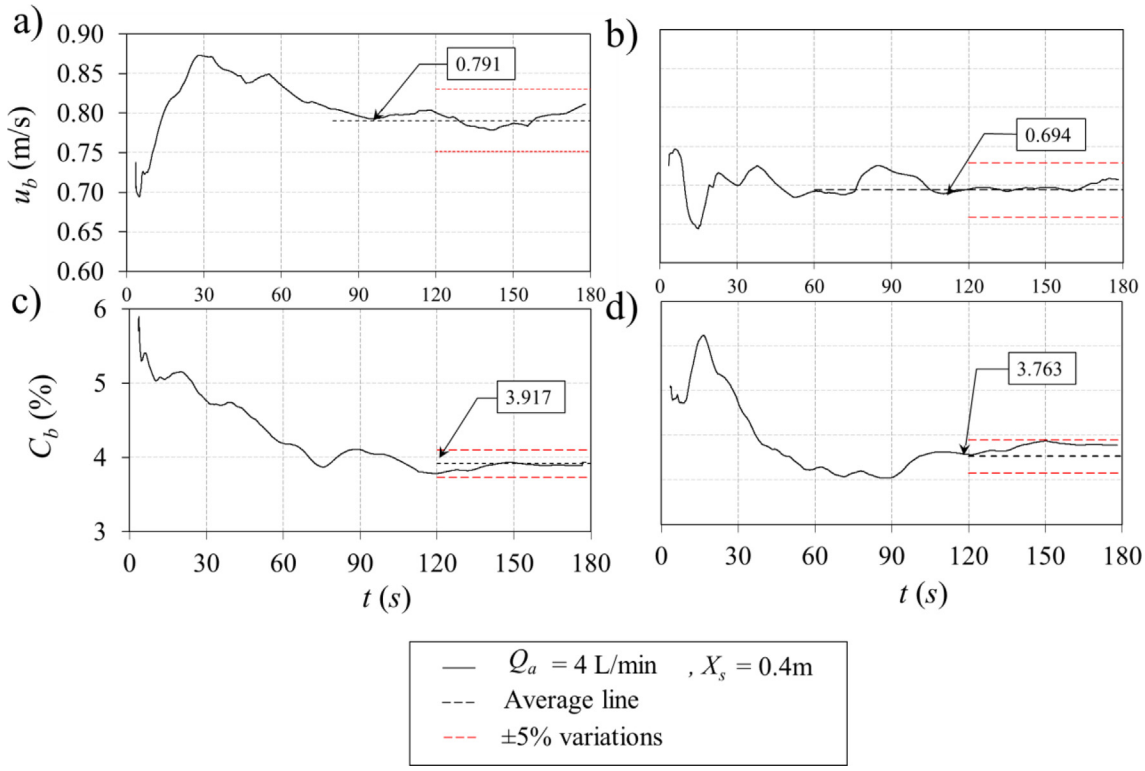

Fig. 3. Time histories of the cumulative average of bubble velocity and bubble concentration with and without a grid-screen for Q_a = 4 L/min and at x/d_o = 330: a) variations of the cumulative average of bubble velocity without a grid-screen (Test No. 1); b) variations of the cumulative average of bubble velocity with a grid-screen for d_s = 2.38 mm, X_s = 0.4 m (Test No. 7); c) variations of the cumulative average of bubble concentration without a grid-screen (Test No. 1); d) variations of the cumulative average of bubble concentration with a grid-screen for d_s = 2.38 mm, X_s = 0.4 m (Test No. 7).

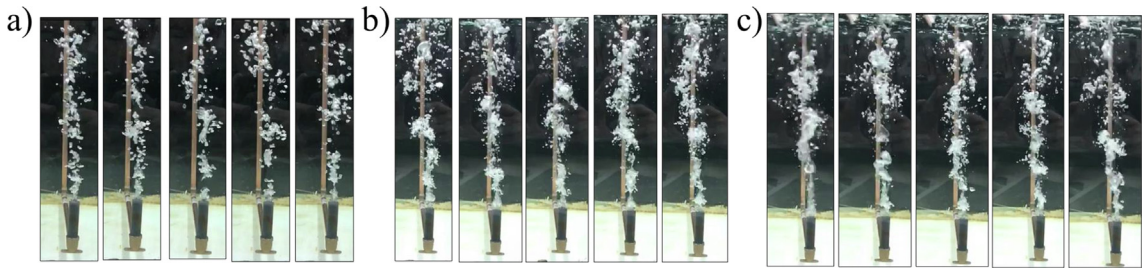

Fig. 4. Images of bubble plume variations with time for the plume tests without a grid-screen and for d_o = 1 mm. The time step between each image is two seconds: a) Q_a = 4 L/min, (Test No. 1); b) Q_a = 6 L/min (Test No. 2); c) Q_a = 8 L/min, (Test No. 3).

Fig. 5. Effect of grid-screen on bubble breakup at different distances from the nozzle for Q_a = 4 L/min, d_o = 1 mm: a) bubble plume without a grid-screen; b) bubble plume with a grid-screen, d_s = 0.841 mm, X_s = 0.14 m.

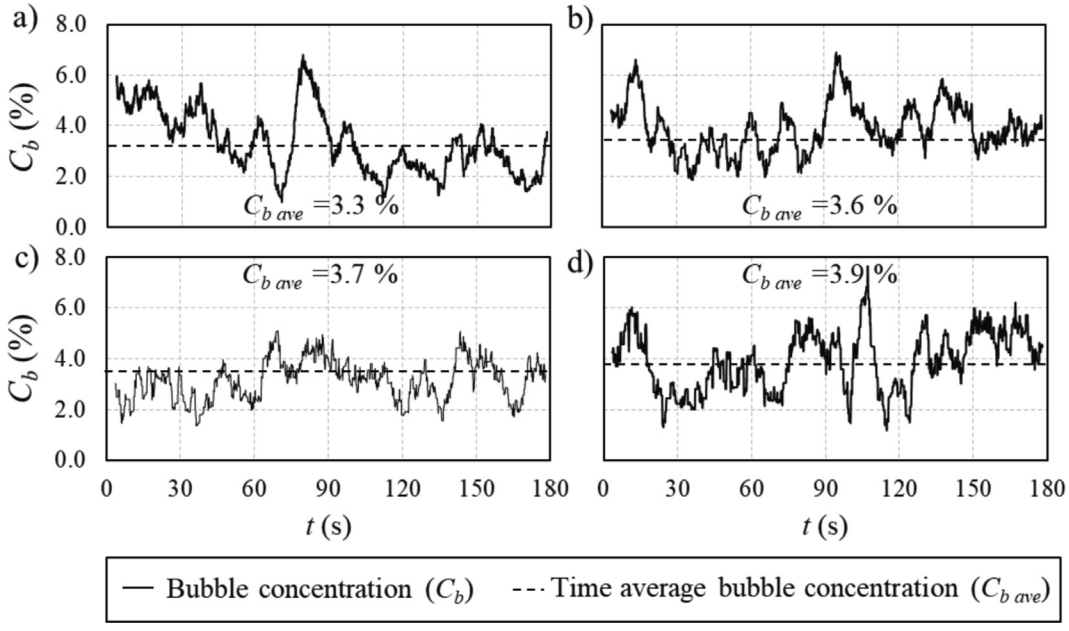

Fig. 6. Time-histories of bubble concentration with and without a grid-screen for Q_a = 4 L/min, d_o = 1 mm, d_s = 2.38 and at x/d_o = 330: a) bubble plume without a grid-screen, (Test No.1); b) bubble plume with a grid-screen located at X_s = 0.14 m, (Test No.7) ; c) bubble plume with a grid-screen located at X_s = 0.22 m, (Test No.8); d) bubble plume with a grid-screen located at X_s = 0.30 m, (Test No.9).

the plumes with grid-screens (Fig. 6b–d) indicated that the installation of a grid-screen increased the bubble concentration at the plume centerline. The maximum difference between the time averaged bubble concentration with and without a grid-screen occurred for X_s = 0.30 m (see Fig. 6d) indicating 21% higher time-averaged bubble concentration than the test without a grid-screen. The grid-screen divides large air bubbles into smaller bubbles once they pass through a grid-screen. Consequently, the number of bubbles detected by the RBI probe increased and bubble concentration increased accordingly. Furthermore, the time-averaged bubble concentration was correlated with the distance from the grid-screen, X_s. A comparison of bubble plumes with and without a grid-screen indicated that the centerline time-averaged bubble concentration increased from 10% to 18% as X_s increased from 0.22 m to 0.30 m (see Fig. 6). The fluctuations of bubble concentration were also calculated for plumes with and without a grid-screen. The averaged concentration fluctuations for plumes without a grid-screen was 31.5% of the average bubble concentration. The grid-screen reduced concentration fluctuations by 10% and the values of concentration fluctuations were independent of X_s. Implementing a grid-screen in bubble plumes also reduced the RMS values of bubble concentration from 1.04 to 0.64 for plumes without a grid-screen and with a grid-screen at the elevation X_s = 0.22 m.

Fig. 7 shows the effects of grid-screen on the time history of bubble velocity at the plume centerline and at x/d_o = 330. The time-history of bubble velocity was recorded for 180 s and the time-averaged bubble velocity, u_{bave}, was calculated and shown by the dotted lines in Fig. 7. The nozzle diameter and air discharge were the same as the bubble plumes presented in Fig. 6. Fig. 7a shows the time-history of bubble velocity for a bubble plume without a grid-screen and Fig. 7b–d show the time-histories of bubble velocities after passing through a grid-screen with different distances from the nozzle, X_s = 0.14 m, 0.22 m, 0.3 m, respectively.

The time-averaged bubble velocity predicted by Bombardelli et al. (2007) was also included in the bubble plume test without a grid-screen (see Fig. 7a) indicating a good correlation between the measured and predicted bubble velocity with only 2.2% difference. A comparison of the time-averaged bubble velocities after the grid-screen indicated that the position of the screen decreased the time-averaged bubble velocity by approximately 24%. The velocity fluctuations were calculated for both cases of with and without grid-screen. The Root-Mean-Square (RMS) values of bubble velocity reduced from 0.116 to 0.076 for bubble plumes without grid-screen and with a grid-screen at X_s = 0.3 m, respectively. As shown in Fig. 7, the time-averaged bubble velocity decreased by approximately 31% due to the presence of a grid-screen located at X_s = 0.3 m. It was found that the bubble velocity fluctuations are correlated with the distance between the grid-screen and the nozzle, X_s. The average velocity fluctuations for bubble plumes without a grid-screen was 13.3% and it decreased to 8.6% in the presence of a grid-screen at X_s = 0.14 m. Bubble velocity fluctuations increased as the distance between grid-screen and nozzle increased to 9.5% and 11.3% for X_s = 0.22 m and 0.3 m, respectively.

The experimental study of Lima Neto et al. (2008a) indicated that the effect of nozzle size is negligible on variations of bubble velocity. Our experimental results indicated that not only bubble size decreased (i.e., bubble concentration increased) but also the velocity of bubbles decreased after the presence of a grid-screen. Bubble size, interfacial area, *a*, and bubble velocity influence the rate of oxygen transfer from bubbles to the ambient water. Mueller et al. (2002a,b) reported an equation derived from Fick's law to show the relationship between bubble characteristics and oxygen transfer rate as:

$$\frac{dC}{dt} = K_L a(C_s - C) \tag{1}$$

where C is dissolved oxygen (DO) concentration in the ambient water; C_s is the saturation concentration of dissolved oxygen, and K_L is mass transfer coefficient or liquid film coefficient. The interfacial area of bubbles is directly correlated with the number of bubbles, bubble size, and bubble velocity. The rate of oxygen transfer increases as a result of bubble velocity reduction and increasing the residence time of bubbles (Clift et al., 1978).

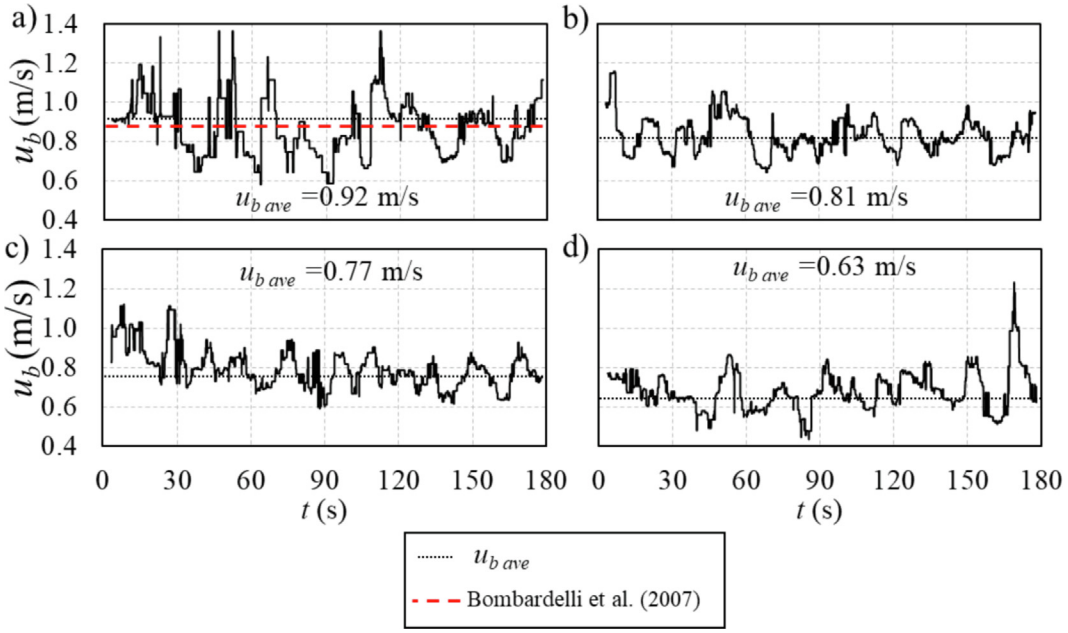

Fig. 7. Time-histories of bubble velocity with and without a grid-screen for Q_a = 4 L/min, d_o = 1 mm, d_s = 2.38 mm and at x/d_o = 330: a) bubble plume without a grid-screen (Test No.1); b) bubble plume with a grid-screen located at X_s = 0.14 m, (Test No.7); c) bubble plume with a grid-screen located at X_s = 0.22 m, (Test No.8); d) bubbly plume with a grid-screen located at X_s = 0.30 m, (Test No.9).

2.3. Bubble characteristics

To study the effect of grid-screen on oxygen transfer enhancement, bubble size distribution on the plume axis and after the grid-screen were measured with the RBI probe. The Probability Density Function (PDF) of bubble size was calculated based on the time-series of bubble size measurements with the RBI probe to identify the most probable bubble size and its distribution for different experiments. The bubble dimeters were measured for 120 s and different ranges of bubble sizes from 0.1 mm to 25 mm were sorted after the measurements. The percentage of bubbles in relatively narrow bonds of 0.1 mm thickness were calculated based on the total number of bubbles to generate bubble size distribution curves.

Fig. 8 shows the most probable bubble size and bubble size distribution for bubble plumes with a grid-screen and with an opening size of 2.38 mm for two different air discharges of Q_a = 4 and 6 L/min. The PDF of bubble sizes for a bubble plume without a grid-screen (see Fig. 8a and b) was also calculated for comparison. The grid-screens were installed at X_s = 0.14 m and bubble size distributions were measured for a distance from the nozzle ranging from 0.16 m to 0.5 m (i.e., $1.15 \leq x/X_s \leq 3.6$). The magnitude of the most probable bubble size provides an insight in uniformity of bubble size after the grid-screen. In addition, the PDF data show the effects of air discharge and grid-screen size on bubble size distribution at different distances from the nozzle. Each subplot shows the probability of bubble size in percentage from the smallest to the larges measured bubbles. A comparison of the calculated PDF for bubble plume without and with a grid-screen at × = 0.16 m (see Fig. 8a and c) indicated the repeatability of the bubble size measurements since the measurement in Fig. 8c was taken before the grid-screen. The most probable bubble size was 6.1 mm ± 2 mm and the PDF of bubble size varied by ± 8.2%.

From the results presented in Fig. 8, it can be concluded that the most probable bubble size after the grid-screen decreased as all peak values of the PDF shifted toward the lower values of d_b. This

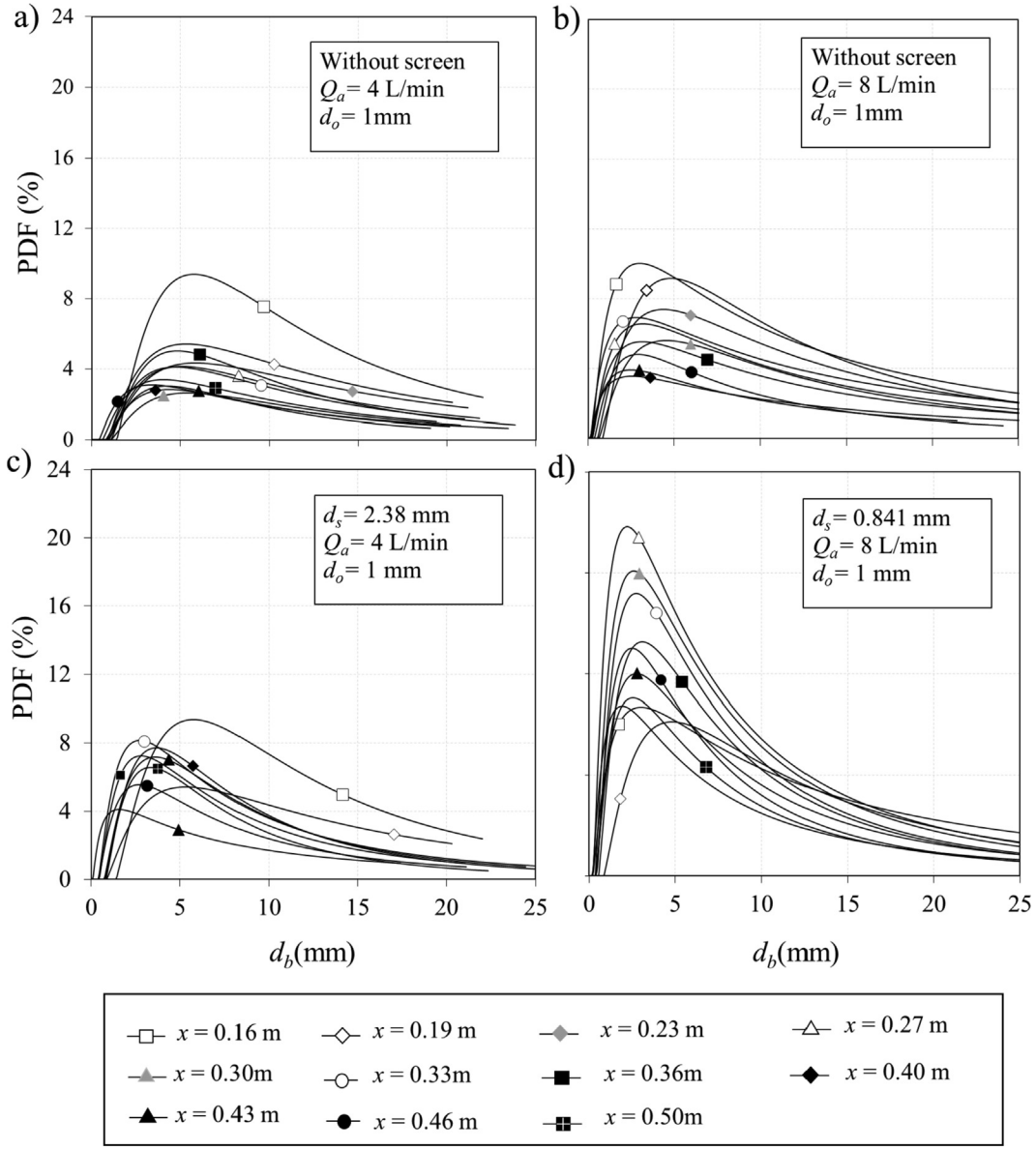

Fig. 8. Effects of grid-screen on the Probability Density Function (PDF) of bubble size in bubble plumes with different discharges, screen sizes, and distances from the nozzle: a) Q_a = 4 L/min, d_o = 1 mm, without a grid-screen (Test No.1); b) Q_a = 6 L/ min, d_o = 1 mm, without a grid-screen (Test No.2); c) Q_a = 4 L/ min, d_o = 1 mm, d_s = 2.38 mm, X_s = 0.14 m, (Test No.7); d) Q_a = 6 L/ min, d_o = 1 mm, d_s = 2.38 mm, X_s = 0.14 m, (Test No.10).

indicates more uniform bubble size distribution and smaller bubble diameters due to the placement of grid-screens. The peak values in probability curves increased after the grid-screen indicating that the resulted bubbles became uniform. The distributions of bubble size before a grid-screen were in good agreement with the observations of Lima Neto et al. (2008a). Their results showed that by replacing a single nozzle with an air-stone, bubble diameters decreased by approximately 50% and the size distribution curves became sharper that indicates the formation of relatively uniform bubble size distribution. A comparison between Fig. 8a and c shows that the most probable bubble size in bubble plumes without a grid-screen decreased from 5 mm to 3.7 mm. Due to installation of a grid-screen the peak probability range increased from 2.5% – 5% to 4% – 7%. Experimental results indicated that by installation of grid-screen not only bubble size decreased but also more uniform bubbles were formed.

Fig. 8b and 8d show the effect of grid-screen in bubble plumes with higher airflow rate. A comparison between Fig. 8a and b shows the effect of airflow discharge on bubble size and its distribution. As can be seen bubble size decreased by increasing airflow rate and the peak bubble size for x = 0.3 m decreased by 19% as the airflow discharge doubled. Our results on variations of the most probable bubble size and bubble size distribution were consistent with the recent studies in the literature (Ziegenhein and Lucas, 2017; Bohne et al., 2020). A comparison between bubble plumes with and without grid-screen in higher air discharges (see Fig. 8c and d) indicated that the peak probability of bubbles at x = 0.33 m increased from 8% to approximately 15%.

Fig. 9 shows the effect of grid-screen on the total number of bubbles, N_b, that were detected by the RBI probe at each point. In order to compare the effect of grid-screen on bubble characteristics, two tests were shown based on the presence of grid-screen placed at X_s = 0.14 m above the nozzle and the benchmark test without a grid-screen. Fig. 9a shows the variations of the total number of bubbles along the axis of the bubble plume for a constant air discharge of Q_a = 4 L/min. The number of bubbles decreased almost linearly with normalized distance from the nozzle. As can be seen, the effect of grid-screen on the total number of bubbles is insignificant for small air discharge and the total number of bubbles increased by approximately 6% in presence of a grid-screen. Fig. 9b shows the variations of N_b with x/d_o for higher air discharge of Q_a = 6 L/min. As can be seen, the total number of bubbles increased by approximately 30% in presence of a grid-screen for relatively higher air discharge.

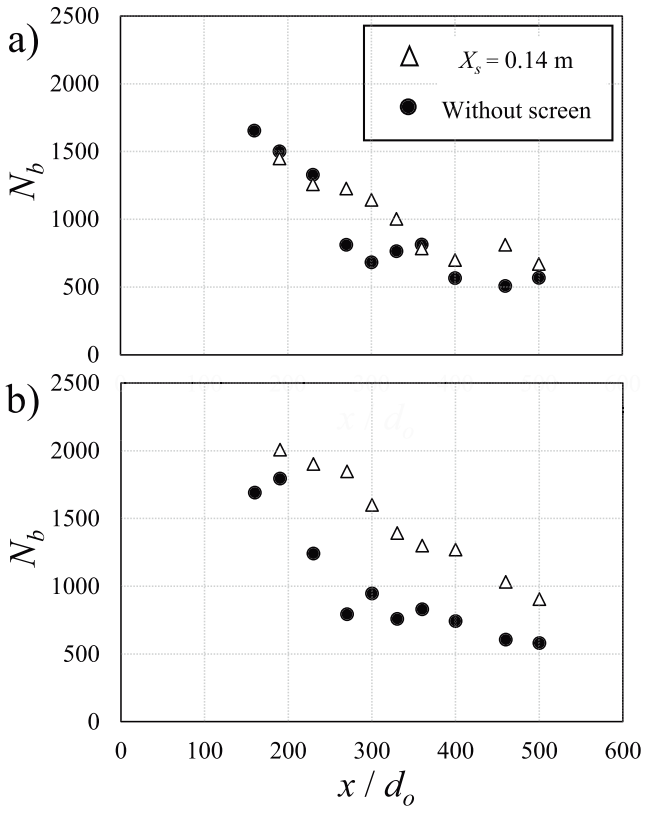

Fig. 9. Effects of grid-screen on the total number of bubbles detected by the RBI probe, N_b: a) Q_a = 4 L/min, d_o = 1 mm, without a grid-screen (Test No.1) and X_s = 0.14 m, (Test No.7); b) Q_a = 6 L/ min, d_o = 1 mm, without a grid-screen (Test No.2) and X_s = 0.14 m, (Test No.10).

Due to constant air discharge of 4 L/min, a comparison between the tests with and without a grid-screen indicated that by increasing the elevation from the nozzle, the number of bubbles decreased which indicated no significant variations between the number of bubbles with and without grid-screen. However, by increasing the air discharge to 6 L/min (see Fig. 9b), the number of bubbles raised significantly after the grid-screen.

The effects of grid-screen on bubble characteristics of bubble plumes are investigated by comparing the variations of bubble size and bubble velocity along the vertical axis of the bubble plume. The variations of bubble size along the vertical axis of the plume, x, were measured in the centerline of the plume and the results were plotted for bubble plumes with different airflow discharges (see Fig. 10). Fig. 10a and b show the bubble size variations for Q_a = 4 L/min, and Fig. 10c,d and 10e-10f show the bubble size variations for Q_a = 6 L/min and 8 L/min, respectively. The left and right subplots in Fig. 10 show the bubble size variations for d_o = 1 mm and 3 mm, respectively. The horizontal lines show the locations of grid-screens at different levels of X_s = 0.14 m, 0.22 m, and 0.3 m. All data points for bubble plumes without a grid-screen are shown by solid circle symbols. The white and grey symbols represent the data for the grid-screen opening of d_s = 2.38 mm and 0.841 mm, respectively. The uncertainty overbars for measuring bubble size are added in Fig. 10. Similar uncertainty ranges with an average value of ± 1.5% were found for other tests.

A comparison between the bubble plumes with and without a grid-screen indicated that the grid-screen significantly reduced the bubble size after the grid-screen. It was found that the bubble size reduction was independent of the screen size or the location of grid-screen. The vertical variations of bubble size in bubble plumes without a grid-screen show that the bubble diameter decreased almost linearly with vertical distance from the nozzle with an average slope of $d(d_b)/dx = -77.7$. Fig. 10 shows that the grid-screens decreased the averaged bubble size right above the grid-screen by approximately 45 percent. However, the effect of nozzle size on variations of bubble size was limited to ± 4.6 %. The effect of grid-screen size on variations of bubble size became important in bubble plume with the lowest Reynolds number, R_e = 5662 (see Fig. 10a). The average bubble size after the grid-screen with d_s = 2.38 mm was 7.5 mm and it decreased to 5 mm as the screen openings decreased from 2.38 mm to 0.84 mm. Such bubble sizes are useful for aeration and de-stratification of tropical reservoirs (Sahoo and Luketina, 2006). In bubble plumes with higher Reynolds number, the effect of screen opening became insignificant. This is consistent with the results of Lima Neto et al. (2008b), in which bubble breakup prevailed for Re > 8000, producing smaller bubbles and a more uniform bubble size distribution.

The effect of air discharge on variation of bubble size was studied by comparing the results presented in Fig. 10a, c, and e. The effect of grid-screen on bubble size reduction was more pronounced in bubble plumes with higher air discharge (i.e., Q_a = 8 L/min). The bubble diameter ranged between 5.8 mm and 7.2 mm in bubble plume with Q_a = 4 L/min and bubble sizes

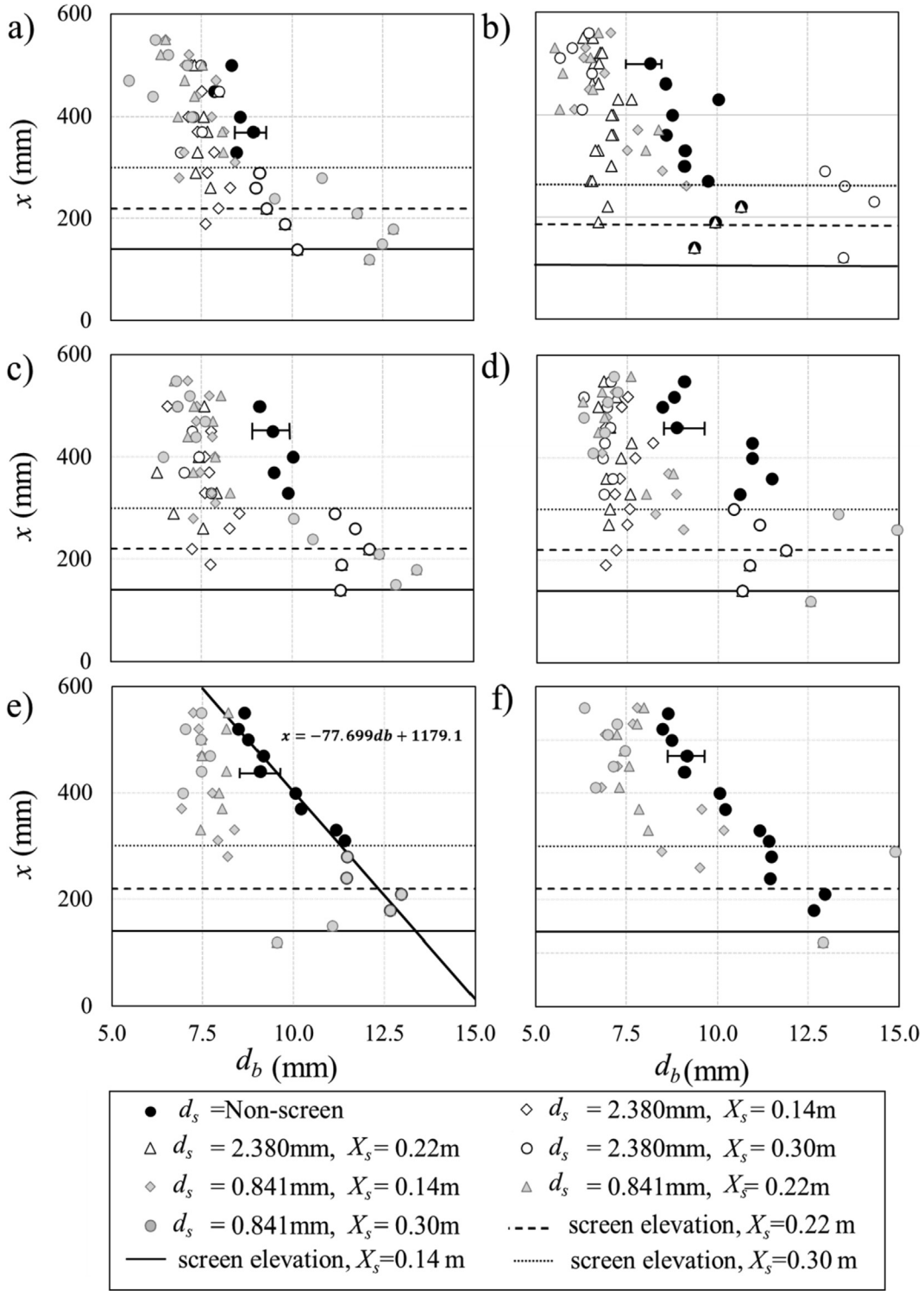

Fig. 10. Variations of bubble size along the vertical axis of bubble plumes with different air discharges, Q_a, nozzle diameters, d_o, and grid-screen sizes, d_s, for a screen located at X_s = 0.14 m, 0.22 m, and 0.30 m: a) Q_a = 4 L/min, d_o = 1 mm, Re = 5661.71; b) Q_a = 4 L/min, d_o = 3 mm, Re = 1887.23; c) Q_a = 6 L/min, d_o = 1 mm, Re = 8492.56; d) Q_a = 6 L/min, d_o = 3 mm, Re = 2830.85; e) Q_a = 8 L/min, d_o = 1 mm, Re = 11323.42; f) Q_a = 8 L/min, d_o = 3 mm, Re = 33970.

increased to a range between 6.7 mm and 8.4 mm by increasing air discharge from 4 L/min to 6 L/min. The effect of grid-screen on bubble size distribution was noticeable in relatively lower air discharge (i.e., Q_a = 4 L/min) and far from the nozzle (i.e., x/d_o = 550). At x/d_o = 550, the average bubble size decreased by 32% as grid-screen size, d_s, reduced from 2.38 mm to 0.84 mm. The grid-screens were located in three different elevations of X_s = 0.14 m, 0.22 m, and 0.33 m, as indicated by dashed and dotted lines in Fig. 10. Bubble sizes in bubble plumes without a grid-screen decreased linearly with the vertical distance from the nozzle whereas bubble sizes in bubble plumes with a grid-screen were constant along the plume axis. As can be seen in Fig. 10, the size of bubbles in bubble plumes with and without a grid-screen became similar far from the nozzle. This indicates that the efficiency of grid-screens in reducing the bubble size is suitable at a certain distance above the screen and a series of grid-screens

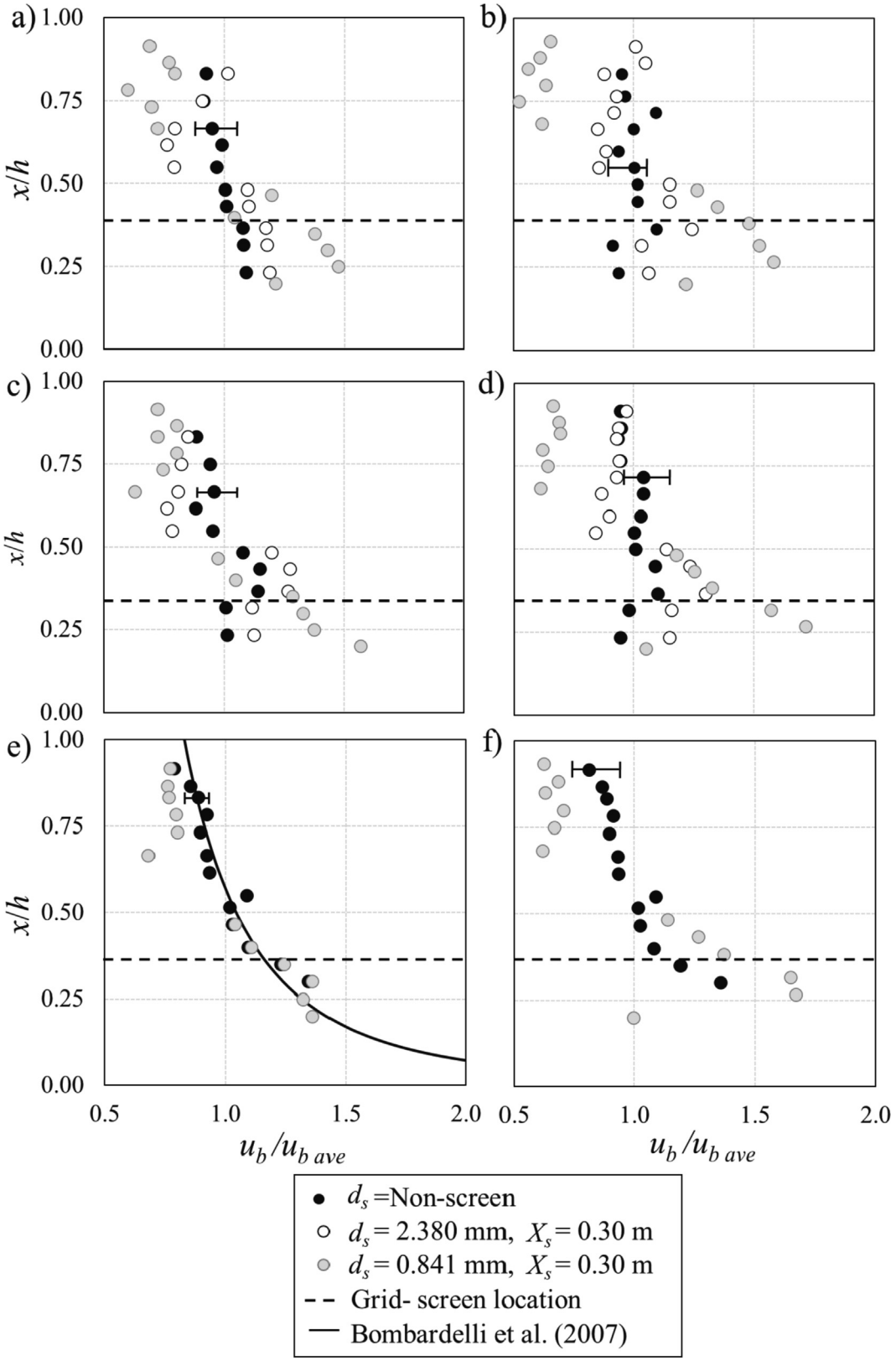

Fig. 11. Variations of the normalized bubble velocity with normalized vertical distance from the nozzle in bubble plumes with different air discharges, Q_a, nozzle sizes, d_o, and grid-screen sizes, d_s. The grid-screen was located at X_s = 0.30 m: a) Q_a = 4 L/min, d_o = 1 mm; b) Q_a = 4 L/min, d_o = 3 mm; c) Q_a = 6 L/min, d_o = 1 mm; d) Q_a = 6 L/min, d_o = 3 mm; e) Q_a = 8 L/min, d_o = 1 mm; f) Q_a = 8 L/min, d_o = 3 mm.

may require for further improvement of oxygen transfer. Although bubbles after a grid-screen eventually reached a relatively similar size than that bubbles without a grid-screen; however, the magnitude of PDF (as shown in Fig. 8) indicated that the resultant bubbles are more uniform after the grid-screen. By employing the linear bubble size reduction in bubble plumes without a grid-screen, bubble size in bubble plumes with and without a grid-screen reached the same sizes at $x/d_o = 310$ and 550 for $Q_a = 4$ L/min and 8 L/min, respectively.

Relatively large bubbles were measured before the grid-screens. This indicates that the bubbles were accumulated under the grid-screen and form forced bubble coalescence. As can be seen in Fig. 10, by increasing the screen elevation, X_s, from 0.14 m to 0.30 m, the bubbles under the screen merged due to bubble velocity reduction. The forced bubble coalescence increased the bubble size by approximately 19% of the bubble size in tests without a grid-screen. This can be confirmed by the time-history of bubble velocity as presented in Fig. 7. In bubble plumes with a grid-screen size of $d_s = 0.841$ mm and with different distances from the nozzle, X_s, bubble diameters after the grid-screen decreased from the benchmark test by approximately 22%.

To study the effect of grid-screen on bubble velocity, the vertical variations of bubble velocity were plotted for bubble plumes with different nozzle sizes and air discharges. The grid-screen size has multiple effect on the averaged bubble velocity. The velocity of bubbles reduced by reducing the bubble size due to smaller buoyancy force and grid-screens with smaller screen size also reduce the momentum flux of the carrier fluid, which can reduce the mean and turbulence momentum transfer between air bubbles and the carrier fluid. The experimental results on vertical variations of bubble velocity with different grid-screen sizes and for the maximum grid-screen elevation of $X_s = 0.30$ m are shown in Fig. 11. Fig. 11 shows the variations of bubble velocity, u_b, normalized with the averaged bubble velocity along the vertical axis, u_{ave}, with the normalized vertical distance from the nozzle, x/h. The proposed model for prediction of bubble velocity in bubble plumes by Bombardelli et al. (2007) was added in Fig. 11e for comparison and validation of the experimental data. As can be seen in Fig. 11, the centerline velocity scales with $x^{-1/3}$ in bubble plumes with relatively high air discharges (Fisher and Honda, 1979; Lai and Socolofsky, 2019; Bomabardelli et al., 2007).

Despite bubble size, the effect of grid-screen size on variations of bubble velocity was significant. As can be seen in Fig. 11a–d, by decreasing the grid-screen size from 2.38 mm to 0.841 mm normalized bubble velocity decreased by 14% and 38% for nozzle size $d_o = 1$ mm and 3 mm, respectively. Such variations showed that increasing the nozzle size caused the air to move through the water with a higher velocity and smaller bubble diameter, which can improve the oxygen transfer after the grid-screen.

The accumulation of bubbles below the grid-screen increased with increasing air discharge. The bubble size below the grid-screen raised due to bubble coalescence and increased the averaged bubble velocity in comparison with bubble velocity without a grid-screen by 52%, 43%, and 23% for air discharges of 4 L/min, 6 L/min, and 8 L/min, respectively (see Fig. 11). Fig. 12 shows the images of bubble coalescence before and after the grid-screen for different air discharges. A comparison of bubble sizes for bubble plumes before and after the grid-screen indicated that the accumulation of bubbles occurred below the grid-screen while significant bubble size reduction occurred after the grid-screen.

2.4. Regime classification

Detailed observations on variations of bubble velocity along the vertical axis resolved four flow regimes. Fig. 13a shows the vertical variations of normalized bubble velocity with normalized distance

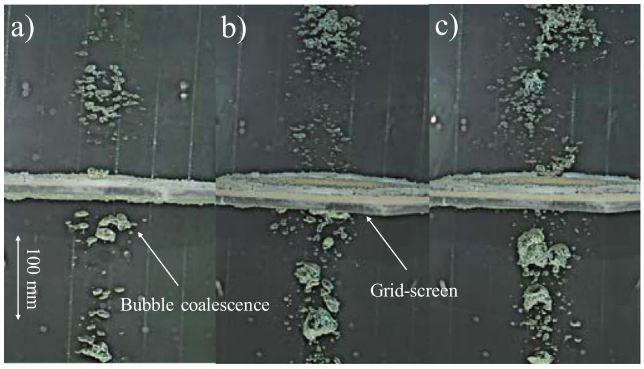

Fig. 12. Snapshot images of bubbles before and after a grid-screen with $d_s = 0.841$, $X_s = 0.22$ m, $d_o = 1$ mm, and different air discharges: a) $Q_a = 4$ L/min, (Test No. 20); b) $Q_a = 6$ L/min (Test No. 23); c) $Q_a = 8$ L/min, (Test No. 26).

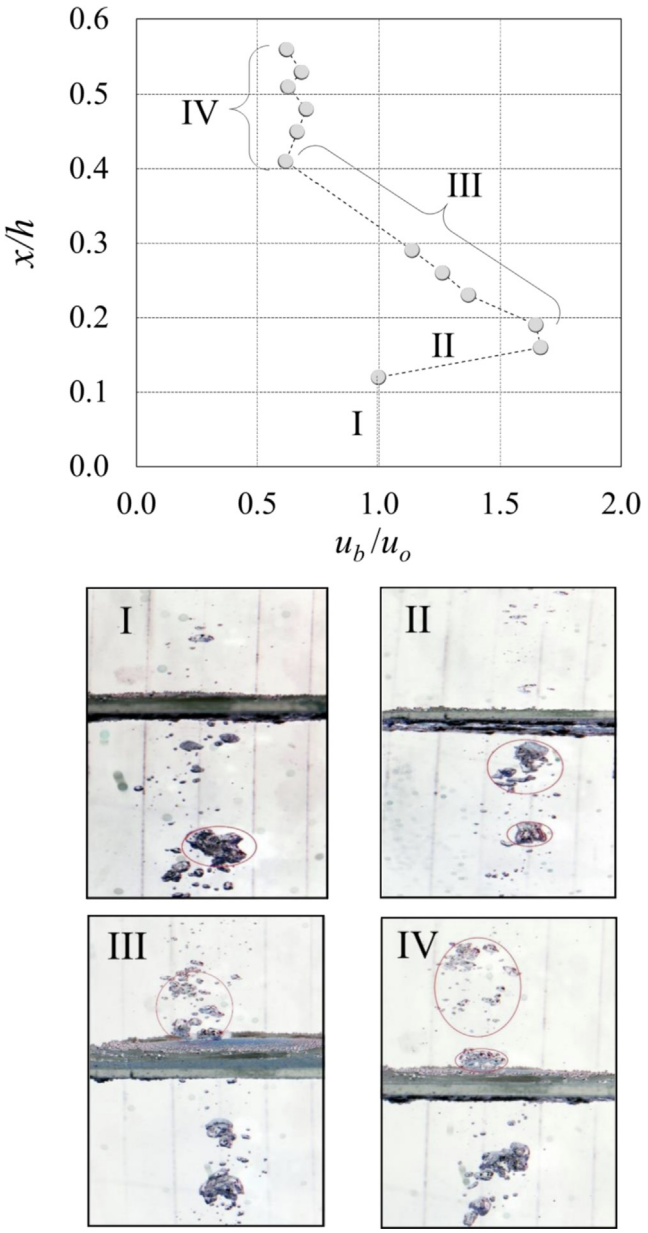

Fig. 13. Regime classification in bubble plumes passing through a grid-screen. The classification is defined based on bubble velocity variations and distance from the nozzle (Test No.7, BP1-4–16).

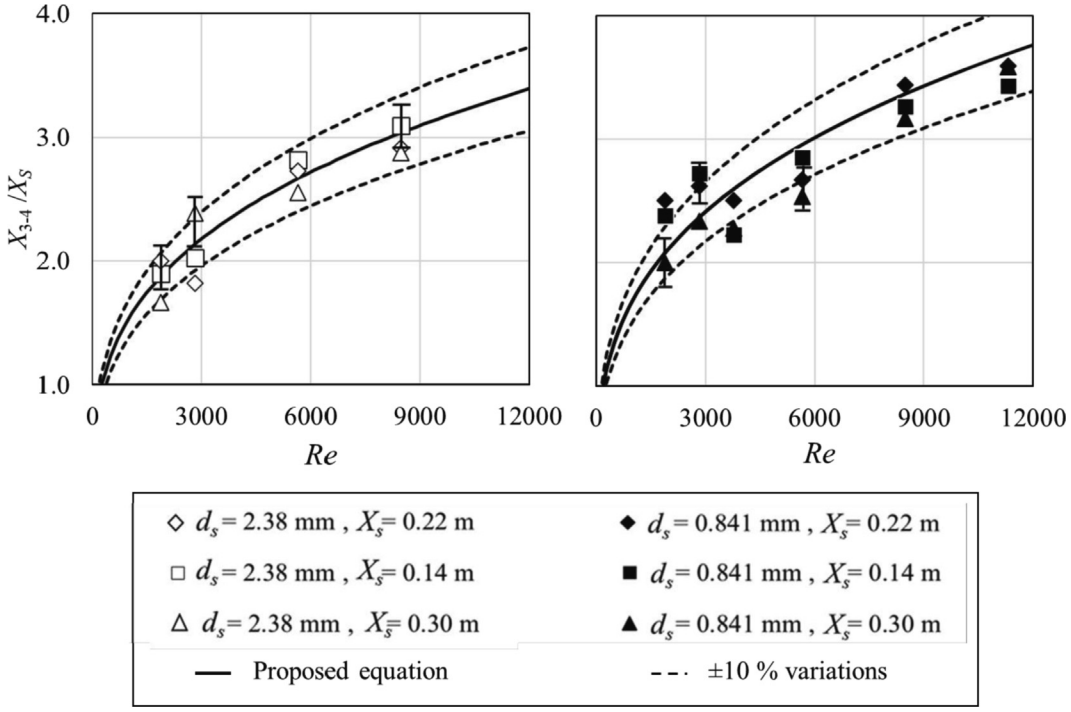

Fig. 14. The correlation of boundary height between regimes (III) and (IV) and Nozzle Reynolds number for bubble plumes passing through a grid screen: a) d_s = 2.38 mm; b) d_s = 0.841 mm.

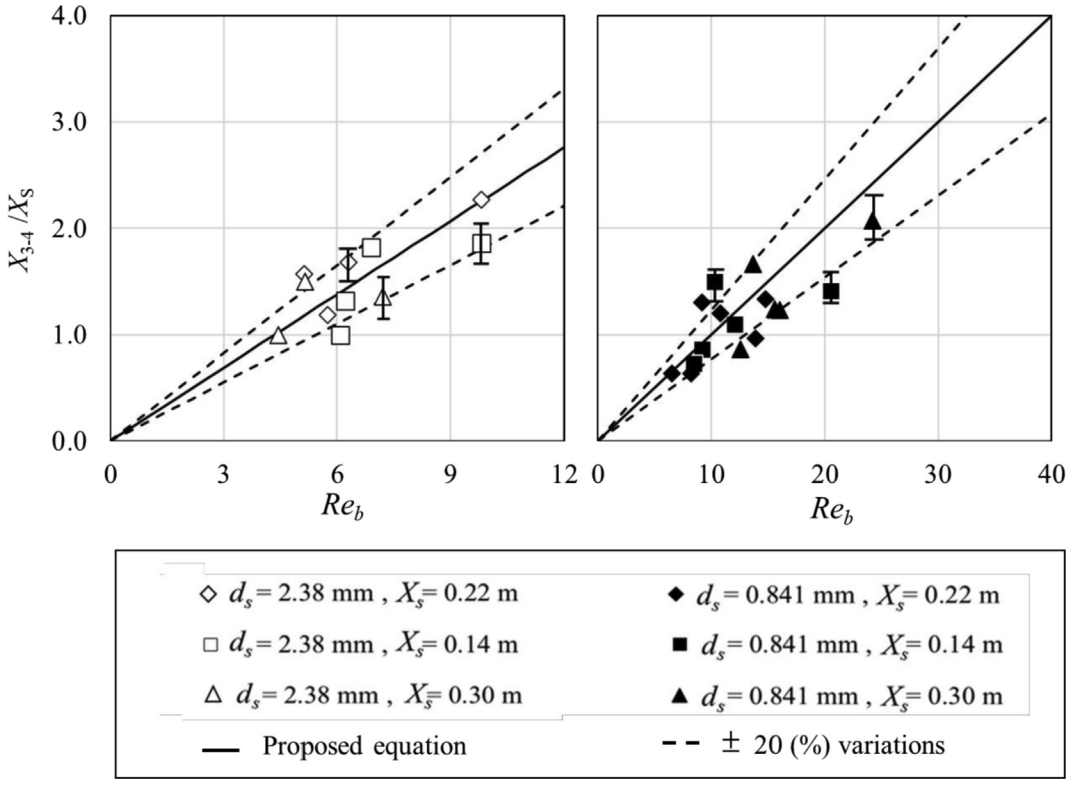

Fig. 15. The correlation of boundary height between regimes (III) and (IV) and Bubble Reynolds number for bubble plumes passing through a grid screen: a) d_s = 2.38 mm; b) d_s = 0.841 mm.

from the nozzle, x/h, for test BP-1–4–16 as a representative of other tests to identify the proposed flow regimes. In this figure, bubble velocities were normalized with the initial jet velocity, u_o. The first regime (Regime *I*) is formed near the nozzle and is defined when bubble velocity is comparable with the initial jet velocity (i.e., $u_b/u_o \approx 1$). As bubbles move up far from the nozzle, their velocities increase due to positive buoyancy force (Regime *II*). As bubbles passed the grid-screen, the screen openings break the boundary

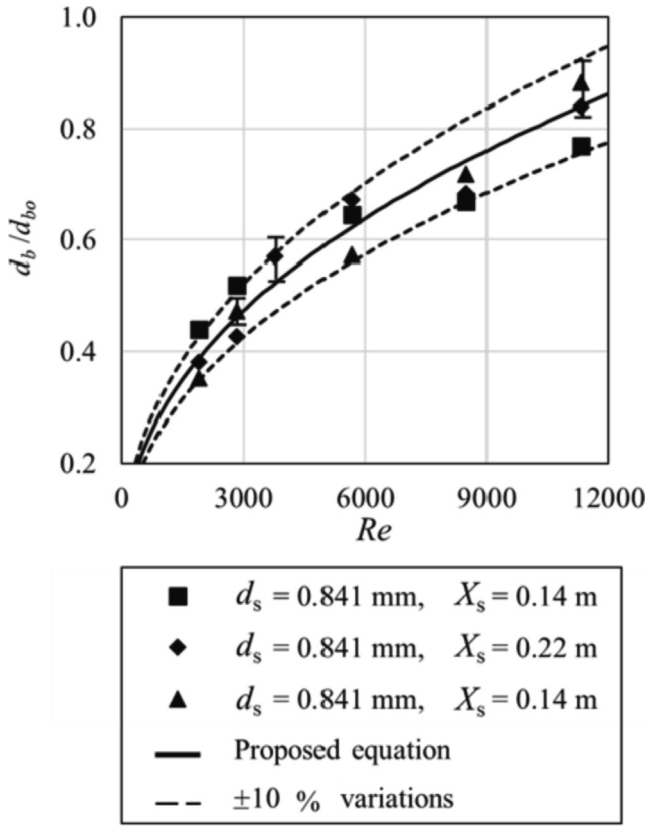

Fig. 16. Effect of screen size on correlation of the normalized nozzle diameter at the boundary of regimes (III) and (IV) with Reynolds number in bubble plumes with different grid-screen elevations.

of the bubbles and increase the number of bubbles as well (see Fig. 9). Consequently, due to the larger contact area in break up bubbles, the energy dissipation after the grid-screen increased significantly. As a result of force imbalance after the grid-screen, bubble velocity decreased until reached the equilibrium velocity. The region of velocity decay after the grid-screen is labeled as Regime *III*. The split bubbles merged due to bubble coalescence and reached the equilibrium velocity in Regime IV. Fig. 13 shows the snapshot images of bubbles at different flow regimes for Test BP1-4–16.

The boundary between regimes three and four, $X_{3\text{-}4}$, is defined as a distance from the nozzle to the point that regime (IV) begins. Experimental results indicated that at this distance, bubble velocities became approximately 85% of the initial bubble velocity. The boundary between regimes three and four, $X_{3\text{-}4}$, corresponds to the time residence of bubbles. To improve oxygen transfer efficiency in bubble plumes, a new grid-screen is required at $X_{3\text{-}4}$. Fig. 14 shows the effects of the distance between grid-screen and nozzle, X_s, and initial Reynolds number Re, on variations of the boundary between regime three and four, $X_{3\text{-}4}$. Fig. 14 shows the capacity of grid-screens to reduce bubble velocity in which such capacity increased with increasing the initial Reynolds number.

The boundary between regimes three and four is affected by nozzle size and air discharge. It is deduced that increasing air discharge and decreasing nozzle diameter raise the height of the regime (*III*). Two equations are proposed to predict the position of the second layer of grid-screen. Eq. (2) is suitable for bubble plumes with a grid-screen opening of d_s = 2.38 mm and Eq. (3) is suitable for the tests with a grid-screen opening of d_s = 0.841 mm.

$$\left(\frac{x_{3-4}}{x_s}\right) = 0.168(\mathrm{Re}^{0.32}) \tag{2}$$

$$\left(\frac{x_{3-4}}{x_s}\right) = 0.1846(\mathrm{Re}^{0.32}) \tag{3}$$

The coefficients of determination, R^2, for Eqs. (2) and (3) are 0.91 and 0.93, respectively. The ± 10% variations of the empirical correlations were also added to Fig. 13, indicating that almost all data points are within ± 10% variations.

Fig. 15 shows the effect of distance between grid-screen and nozzle, X_s, and bubble Reynolds number, Re_b, on variations of the boundary between regime three and four, $X_{3\text{-}4}$. Bubble Reynolds number is defined as the ratio of bubble inertial force to water viscous force as $\mathrm{Re}_b = \rho_a u_b d_b/\mu_w$, where u_b is the bubble velocity, d_b is the bubble diameter, ρ_a is the air density, and μ_w is the kinematic viscosity of water. As can be seen in Fig. 15a and b, the distance between grid-screen and nozzle was increased, by increasing the bubble Reynolds number. It was observed that by decreasing the grid-screen size, the correlation slope decreased and lead to higher values of distance between grid-screen and nozzle. Two equations were proposed to predict the boundary between two specified regimes (e.g., regimes three and four). Eq. (4) is for grid-screen size of d_s = 2.38 mm and Eq. (5) is for grid-screen size of d_s = 0.841 mm.

$$\left(\frac{x_{3-4}}{x_s}\right) = 0.23(\mathrm{Re}_b) \tag{4}$$

$$\left(\frac{x_{3-4}}{x_s}\right) = 0.1(\mathrm{Re}_b) \tag{5}$$

The coefficients of determination for Eq. (4) and 5) are 0.92 and 0.91, respectively. The ± 20 % variations of the empirical correlations were also added to Fig. 15, indicating that almost all data points are within ± 20 % variations. It should be noted that the material type of grid-screens might slightly change the variation of data.

Fig. 16 shows the variations of normalized bubble diameter at the beginning of Regime IV with the initial Reynolds number, Re. The results indicated that Reynolds number had negligible impact on the normalized bubble size for the grid-screen with larger openings, d_s = 2.38 mm. On the other hand, for d_s = 0.841 mm the normalized bubble size increased by the initial Reynolds number. It is deduced that small grid-screen caused the bubble plume to reach the regime (IV) at the lower elevations and therefore, a second layer of grid-screen will be beneficial for mixing improvement. A non-linear equation was proposed to correlate the normalized bubble diameter at the onset of regime (IV) with the initial Reynolds number as:

$$\left(\frac{d_b}{d_{bo}}\right) = 0.0149(\mathrm{Re}^{0.43}) \tag{6}$$

The coefficient of determination of Eq. (6) is R^2 = 0.92. The ± 10% variations of the empirical correlations were also added to Fig. 16. The variation curves indicated that almost all data points are within ± 10% variations. Considering measurement uncertainties, it was found that the proposed equation is suitable for prediction of the onset of Regime IV with a reasonable accuracy.

3. Conclusions

A series of laboratory experiments was conducted to investigate the effect of grid-screen and its location on the bubble properties in a circular bubble plume. The RBI bubble probe was employed to

investigate the effects of air discharge on variations of bubble velocity and bubble size after the grid-screen. By installing a grid-screen at 0.3 m above the nozzle, the time-averaged bubble concentration increased by 18% and the time-averaged bubble velocity decreased by approximately 31% in comparison with the benchmark test without a grid-screen. The experimental observations indicated that the installation of a grid-screen not only decrease the bubble sizes but also increase uniformity of bubble size distribution. It was observed that the effect of grid-screen on bubble size reduction was more significant in bubble plumes with higher air discharge. Additionally, the experimental results showed that bubble velocity after the grid-screen decreased as the screen opening decreased.

The velocity of bubbles was measured along the centerline axis of the bubble plumes. The results revealed that total bubble numbers after the grid-screen increased in tests with higher airflow rates (i.e., 6 L/min). This indicated that the bubble diameter decreased along the centerline axis of the plume and above the nozzle. Our observations indicated that the bubble size decreased right after the grid-screen. However, it gradually increased as it moved towards the water surface. A regime classification was introduced based on the variations of bubble velocity along the axis of the plume. Bubble velocity was constant in the first regime near the nozzle. The second regime was defined as the position that bubble velocity increased with distance from the nozzle and it ended at the position of grid-screen. The third regime started from the grid-screen position to the depth where the bubble velocity became constant. Bubble velocity was constant in regime four indicating that the effect of grid-screen was insignificant beyond this depth. The distance from the nozzle to a point where bubble velocity reached the equilibrium was defined as a length scale and it was measured for all cases. It was found that the depth at which the equilibrium velocity occurred is correlated with the bubble Reynolds number. It was found that the normalized bubble size is also correlated with the bubble Reynolds number. Empirical equations were proposed to estimate bubble size and the location of regime boundary, which can be used for designing grid-screen layers and estimation of oxygen transfer after grid-screens.

CRediT authorship contribution statement

Arsalan Behzadipour: Writing – original draft. **Amir H. Azimi:** Conceptualization, Supervision, Writing – review & editing. **Iran E. Lima Neto:** Conceptualization, Writing – review & editing.

Declaration of Competing Interest

This study was financially supported by the Natural Sciences and Engineering Research Council of Canada (NSERC) Discovery Grant No. 421785. The authors are thankful to our lab technician (Mr. Morgan Ellis and Mr. Cory Hubbard) for his support in preparation of a part of the experimental setup.

References

Alméras, E., Mathai, V., Lohse, D., Sun, C., 2017. Experimental investigation of the turbulence induced by a bubble swarm rising within incident turbulence. J. Fluid Mech. 825, 1091–1112.

Aoyama, S., Hayashi, K., Hosokawa, S., Tomiyama, A., 2016. Shapes of ellipsoidal bubbles in infinite stagnant liquids. Int. J. Multiph. Flow 79, 23–30.

Asaeda, T., Imberger, J., 1993. Structure of bubble plumes in linearly stratified environments. J. Fluid Mech. 249, 35–37. https://doi.org/10.1017/S0022112093001065.

Bergmann, C., Seol, D.G., Bhaumik, T., Socolofsky, S.A., 2004. December). Entrainment and mixing properties of a simple bubble plume. In: 4th International Symposium on Environmental Hydraulics, pp. 403–409.

Besbes, S., Gorrab, I., ElHajem, M., Ben Aissia, H., Champagne, J.Y., 2020. Effect of bubble plume on liquid phase flow structures using PIV. Particulate Sci. Technol. 38 (8), 963–972.

Boes, R.M., Hager, W.H., 2003. Two-phase flow characteristics of stepped spillways. J. Hydraul. Eng. 129 (9), 661–670.

Bohne, T., Grießmann, T., Rolfes, R., 2020. Development of an efficient buoyant jet integral model of a bubble plume coupled with a population dynamics model for bubble breakup and coalescence to predict the transmission loss of a bubble curtain. Int. J. Multiph. Flow 132, 103436. https://doi.org/10.1016/j.ijmultiphaseflow.2020.103436.

Bombardelli, F.A., Buscaglia, G.C., Rehmann, C.R., Rincón, L.E., García, M.H., 2007. Modeling and scaling of aeration bubble plumes: A two-phase flow analysis. J. Hydraul. Res. 45 (5), 617–630.

Bormans, M., Maršálek, B., Jančula, D., 2016. Controlling internal phosphorus loading in lakes by physical methods to reduce cyanobacterial blooms: A review. Aquat. Ecol. 50 (3), 407–422.

Bryant, D.B., Seol, D.-G., Socolofsky, S.A., 2009. Quantification of turbulence properties in bubble plumes using vortex identification methods. Phys. Fluids 21 (7), 075101. https://doi.org/10.1063/1.3176464.

Chaumat, H., Billet-Duquenne, A.M., Augier, F., Mathieu, C., Delmas, H., 2005. Application of the double optic probe technique to distorted tumbling bubbles in aqueous or organic liquid. Chem. Eng. Sci. 60 (22), 6134–6145.

Chen, G., Zhang, Z., Gao, F., Li, J., Dong, J., 2021. Effect of Different Configurations on Bubble Cutting and Process Intensification in a Micro-Structured Jet Bubble Column Using Digital Image Analysis. Processes 9 (12), 2220.

Clift, R., Grace, J. R., & Bubbles, M. W., 1978. Drops and particles Academic press. New York.

Fannelop, T.K., 1980. Hydrodynamics of Underwater Blowouts. Norwegian Maritime Res. 4, 7–33.

Fisher, J.B., Honda, H., 1979. Branch geometry and effective leaf: a study of terminaua- branching pattern 1. Theoretical trees. American J. Botany 66 (6), 633–644.

Fraga, B., Stoesser, T., Lai, C.C.K., Socolofsky, S.A., 2016. A LES-based Eulerian-Lagrangian approach to predict the dynamics of bubble plumes. Ocean Model 97, 27–36.

Fraga, B., Stoesser, T., 2016. Influence of bubble size, diffuser width, and flow rate on the integral behavior of bubble plumes. J. Geophys. Res. Oceans 121 (6), 3887–3904.

Funaki, J., Shintani, A., Kawaguchi, R., Hirata, K., 2009. Basic space structure of bubble-jet plume using consecutive 3D-PTV. J. Fluid Sci. Technol. 4 (2), 348–358.

García, C.M., García, M.H., 2006. Characterization of flow turbulence in large-scale bubble-plume experiments. Experim. Fluids 41 (1), 91–101.

Ibelings, B.W., Bormans, M., Fastner, J., Visser, P.M., 2016. CYANOCOST special issue on cyanobacterial blooms: Synopsis— A critical review of the management options for their prevention, control and mitigation. Aquatic Ecol. 50 (3), 595–605.

Iguchi, M., Tani, J. I., Uemura, T., Kawabata, H., Takeuchi, H., & Morita, Z. I., 1989. The characteristics of water and bubbling jets in a cylindrical vessel with bottom blowing. ISIJ International, 29(4), 309-317.

Jain, D., Lau, Y.M., Kuipers, J.A.M., Deen, N.G., 2013. Discrete bubble modeling for a micro-structured bubble column. Chem. Eng. Sci. 100, 496–505.

Kiambi, S.L., Duquenne, A.-M., Dupont, J.-B., Colin, C., Risso, F., Delmas, H., 2003. Measurements of bubble characteristics: comparison between double optical probe and imaging. Canadian J. Chem. Eng. 81 (3-4), 764–770.

Lai, C.C.K., Socolofsky, S.A., 2019. The turbulent kinetic energy budget in a bubble plume. J. Fluid Mech. 865, 993–1041.

Laupsien, D., Cockx, A., Line, A., 2017. Bubble plume oscillations in viscous fluids. Chem. Eng. Technol. 40 (8), 1484–1493.

Laupsien, D., Men, C.L., Cockx, A., Liné, A., 2021. Effects of liquid viscosity and bubble size distribution on bubble plume hydrodynamics. Chem. Eng. Res. Des. https://doi.org/10.1016/j.cherd.2021.09.025.

Lee, J. H., & Chu, V. H., 2003. Turbulent Round Jet in Coflow. In Turbulent Jets and Plumes (pp. 179–209).

Li, G., Wang, B., Wu, H., DiMarco, S.F., 2020. Impact of bubble size on the integral characteristics of bubble plumes in quiescent and unstratified water. Int. J. Multiphase Flow 125, 103230. https://doi.org/10.1016/j.ijmultiphaseflow.2020.103230.

Lima, D.D., Lima Neto, I.E., 2018. Effect of nozzle design on bubbly jet entrainment and oxygen transfer efficiency. J. Hydraul. Eng. 144 (8), 06018010. https://doi.org/10.1061/(ASCE)HY.1943-7900.0001493.

Lima Neto, I.E., 2012. Bubble plume modeling with new functional relationships. J. Hydraul. Res. 50 (1), 134–137.

Lima Neto, I.E., Zhu, D.Z., Rajaratnam, N., Yu, T., Spafford, M., McEachern, P., 2007. Dissolved oxygen downstream of an effluent outfall in an ice-covered river: Natural and artificial aeration. J. Environ. Eng. 133 (11), 1051–1060.

Neto, I.E., Zhu, D.Z., Rajaratnam, N., 2008a. Air injection in water with different nozzles. J. Environ. Eng. 134 (4), 283–294.

Lima Neto, I.E., Zhu, D.Z., Rajaratnam, N., 2008b. Bubbly jets in stagnant water. Int. J. Multiph. Flow 34 (12), 1130–1141.

Lima Neto, I.E., Zhu, D.Z., Rajaratnam, N., 2008c. Horizontal injection of gas-liquid mixtures in a water tank. J. Hydraul. Eng. 134 (12), 1722–1731.

Lima Neto, I.E., Zhu, D.Z., Rajaratnam, N., 2008d. Horizontal injection of gas–liquid mixtures in a water tank. J. Hydraulic Eng. 134 (12), 1722–1731.

Lima Neto, I.E., Cardoso, S.S., Woods, A.W., 2016. On mixing a density interface by a bubble plume. J. Fluid Mech. 802.

Liu, L., Yan, H., Ziegenhein, T., Hessenkemper, H., Li, Q., Lucas, D., 2019. A systematic experimental study and dimensionless analysis of bubble plume oscillations in rectangular bubble columns. Chem. Eng. J. 372, 352–362.

Mantripragada, V.T., Sahu, S., Sarkar, S., 2021. Morphology and flow behavior of buoyant bubble plumes. Chem. Eng. Sci. 229, 116098. https://doi.org/10.1016/j.ces.2020.116098.
McGinnis, D.F., Lorke, A., Wüest, A., Stöckli, A., Little, J.C., 2004. Interaction between a bubble plume and the near field in a stratified lake. Water Resour. Res. 40 (10). https://doi.org/10.1029/2004WR003038.
Milgram, J.H., 1983. Mean flow in round bubble plumes. J. Fluid Mech. 133, 345–376.
Moura, D.S., Lima Neto, I.E., Clemente, A., Oliveira, S., Pestana, C.J., Aparecida de Melo, M., Capelo-Neto, J., 2020. Modeling phosphorus exchange between bottom sediment and water in tropical semiarid reservoirs. Chemosphere 246, 125686. https://doi.org/10.1016/j.chemosphere.2019.125686.
Mueller, J., Boyle, W. C., & Popel, H. J. (2002). *Aeration: Principles and Practice, Volume 11* (Vol. 11). CRC press.
Mueller, J., Boyle, W. C., & Popel, H. J., 2002. Aeration: Principles and Practice, Volume 11. CRC press.
Murzyn, F., Mouaze, D., Chaplin, J.R., 2005. Optical fiber probe measurements of bubbly flow in hydraulic jumps. Int. J. Multiph. Flow 31 (1), 141–154.
Springer, Boston, MA.Niida, Y., & Watanabe, Y., 2018. Oxygen transfer from bubble-plumes. Physics of fluids, 30(10), 107104.
Pacheco, C.H.A., Lima Neto, I.E., 2017. Effect of artificial circulation on the removal kinetics of cyanobacteria in a hypereutrophic shallow lake. J. Environ. Eng. 143 (12), 06017010. https://doi.org/10.1061/(ASCE)EE.1943-7870.0001289.
Paerl, H.W., Otten, T.G., 2013. Harmful cyanobacterial blooms: Causes, consequences, and controls. Microb. Ecol. 65 (4), 995–1010.
Rensen, J., Roig, V., 2001. Experimental study of the unsteady structure of a confined bubble plume. Int. J. Multiph. Flow 27 (8), 1431–1449.
Riboux, G., Risso, F., Legendre, D., 2010. Experimental characterization of the agitation generated by bubbles rising at high Reynolds number. J. Fluid Mech. 643, 509–539.
Roig, V., De Tournemine, A.L., 2007. Measurement of interstitial velocity of homogeneous bubbly flows at low to moderate void fraction. J. Fluid Mech. 572, 87–110.
Rosso, D., Stenstrom, M.K., 2006. Surfactant effects on α-factors in aeration systems. Water Res. 40 (7), 1397–1404.
Sahoo, G.B., Luketina, D., 2006. Response of a Tropical Reservoir to Bubbler Destratification. ASCE, J. Environ. Eng. 132 (7), 736–746.
Schladow, S.G., 1992. Bubble plume dynamics in a stratified medium and the implications for water quality amelioration in lakes. Water Resour. Res. 28 (2), 313–321.
Schladow, S.G., 1993. Lake destratification by bubble-plume systems: Design methodology. J. Hydraul. Eng. 119 (3), 350–368.
Seol, D.-G., Bhaumik, T., Bergmann, C., Socolofsky, S.A., 2007. Particle image velocimetry measurements of the mean flow characteristics in a bubble plume. J. Eng. Mech. 133 (6), 665–676.
Seol, D.-G., Bryant, D.B., Socolofsky, S.A., 2009. Measurement of behavioral properties of entrained ambient water in a stratified bubble plume. J. Hydraul. Eng. 135 (11), 983–988.
Simiano, M., Zboray, R., de Cachard, F., Lakehal, D., Yadigaroglu, G., 2006. Comprehensive experimental investigation of the hydrodynamics of large-scale, 3D, oscillating bubble plumes. Int. J. Multiph. Flow 32 (10-11), 1160–1181.
Singleton, V.L., Gantzer, P., Little, J.C., 2007. Linear bubble plume model for hypolimnetic oxygenation: Full-scale validation and sensitivity analysis. Water Resour. Res. 43 (2). https://doi.org/10.1029/2005WR004836.
Socolofsky, S.A., Adams, E.E., 2002. Multi-phase plumes in uniform and stratified crossflow. J. Hydraul. Res. 40 (6), 661–672.
Socolofsky, S.A., Adams, E.E., 2003. Liquid volume fluxes in stratified multiphase plumes. J. Hydraul. Eng. 129 (11), 905–914.
Socolofsky, S.A., Adams, E.E., 2005. Role of slip velocity in the behavior of stratified multiphase plumes. J. Hydraulic Eng. 131 (4), 273–282.
Soltero, R.A., Sexton, L.M., Ashley, K.I., McKee, K.O., 1994. Partial and full lift hypolimnetic aeration of Medical Lake, WA to improve water quality. Water Res. 28 (11), 2297–2308.
Sujatha, K.T., 2016. Cutting bubbles: an experimental and numerical investigation of micro-structured bubble column. Technische Universiteit Eindhoven, Netherland, p. 138. PhD Thesis.
Sujatha, K.T., Meeusen, B.G.J., Kuipers, J.A.M., Deen, N.G., 2015. Experimental studies of bubbly flow in a pseudo-2D micro-structured bubble column reactor using digital image analysis. Chem. Eng. Sci. 130, 18–30.
Vazquez, A., Sanchez, R.M., Salinas-Rodríguez, E., Soria, A., Manasseh, R., 2005. A look at three measurement techniques for bubble size determination. Exp. Therm. Fluid Sci. 30 (1), 49–57.
Wang, B., Lai, C.C.K., Socolofsky, S.A., 2019. Mean velocity, spreading and entrainment characteristics of weak bubble plumes in unstratified and stationary water. J. Fluid Mech. 874, 102–130.
Wüest, A., Brooks, N.H., Imboden, D.M., 1992a. Bubble plume modeling for lake restoration. Water Resour. Res. 28 (12), 3235–3250.
Wüest, A., Brooks, N.H., Imboden, D.M., 1992b. The hydrodynamics of a subsea blowout. Appl. Ocean Res. 28 (12), 3235–3250.
Yang, D.i., Chen, B., Socolofsky, S.A., Chamecki, M., Meneveau, C., 2016. Large-eddy simulation and parameterization of buoyant plume dynamics in stratified flow. J. Fluid Mech. 794, 798–833.
Yapa, P.D., Zheng, L.i., Nakata, K., 1999. Modeling underwater oil/gas jets and plumes. J. Hydraul. Eng. 125 (5), 481–491.
Ziegenhein, T., Lucas, D., 2017a. Observations on bubble shapes in bubble columns under different flow conditions. Exp. Therm. Fluid Sci. 85, 248–256.
Ziegenhein, T., Lucas, D., 2017b. Observations on bubble shapes in bubble columns under different flow conditions. Exp. Therm. Fluid Sci. 85, 248–256.